Volume 5 Issue 1

MERSIN PHOTOGRAMMETRY JOURNAL

The MERSİN PHOTOGRAMMETRY JOURNAL (MEPHOJ)

THE MERSİN PHOTOGRAMMETRY JOURNAL (MEPHOJ) publishes original and innovative contributions in photogrammetric applications ranging from the integration of instruments, methodologies, and technologies and their respective uses in the environmental sciences, engineering, and other natural sciences. Mersin Photogrammerty Journal is a branch of science that widely applied in many scientific disciplines. MEPHOJ aims to cover the entirety of Photogrammetry and Photogrammetric aplications about Geosciences, including their application domains. MEPHOJ strives to encourage scientists to publish experimental, theoretical, and computational results as detailed as possible so that results can be easily reproduced.

MEPHOJ is a double peer-reviewed (blind) OPEN ACCESS JOURNAL that publishes professional level research articles and subject reviews exclusively in English. It allows authors to submit articles online and track his or her progress via its web interface. All manuscripts will undergo a refereeing process; acceptance for publication is based on at least two positive reviews. The journal publishes research and review papers, professional communication, and technical notes. MEPHOJ does not charge for any article submissions or for processing.

CORRESPONDENCE ADDRESS
Journal Contact: myakar@mersin.edu.tr

CONTENTS

Volume 5 - Issue 1

RESEARCH ARTICLES

Mersin Photogrammetry Journal
https://dergipark.org.tr/en/pub/mephoj
e-ISSN 2687-654X

Effect of denoising methods for hyperspectral images classification: DnCNN, NGM, CSF, BM3D and Wiener

Mehmet Akif Günen [*1], **Erkan Besdok** [2]

[1]*Gümüşhane University, Department of Geomatics Engineering, Türkiye*
[2]*Erciyes University, Department of Geomatics Engineering, Türkiye*

Keywords
Denoising
Remote sensing
Hyperspectral
Classification

Research Article
DOI:10.53093/mephoj.1213166

Received:01.12.2022
Revised:23.02.2023
Accepted:27.02.2023
Published:27.05.2023

Abstract

Hyperspectral images are widely used for land use/cover analysis in remote sensing due to their rich spectral information. However, these data often suffer from noise caused by various factors such as random and systematic errors, making them less useful for end-users. In this study, denoising methods (i.e., DnCNN, NGM, CSF, BM3D, and Wiener) for hyperspectral images were compared using the Pavia University hyperspectral dataset with four different noise types: Gaussian, Salt & Pepper, Poisson, and Speckle. After denoising, the k-nearest neighbor method was used to classify the image, and statistical and visual performance comparisons were performed on the classified data. Six performance metrics -Accuracy, Sensitivity, Specificity, Precision, F-Score, and G-Mean- were employed to compare the outcomes qualitatively. The findings demonstrate that DnCNN and BM3D have the best outcome performance for all four noise types. Due to their lack of sensitivity and specificity, the CSF and Wiener approaches had low performance for particular noise sources. For all noise types, the NGM approach had the worst results. The validated instruments not provide effective results when it came to denoising Salt & Pepper noise, but they managed to produce outstanding results when it came to denoising Poisson noise. In order to enhance the quality and usability of hyperspectral images for land use/cover analysis, this study emphasizes the significance of choosing an effective denoising technique.

1. Introduction

Hyperspectral images (HSI) are significant data that can be successfully employed in many different industries, such as agriculture, astronomy, and the military, including remote sensing and photogrammetry, because they contain significantly more spectral information than three-band red, green, and blue (RGB) images. The number of photons captured per band is much lesser in HSIs than in RGB images, allowing different noises to be easily incorporated into the corresponding bands during the acquisition process. This is because HSIs capture the spectral information of each spatial location in a scene with large wavebands [1-3]. These noises cause image distortions, which have a detrimental effect on the performance of all HSI applications as well as how the HSI is visually presented. An important stage in the analysis and processing of HSI is denoising. The multi-detector imaging method of HSI sensors, however, results in complex noises like random noise and structural stripe noise. Through advanced analysis, this complex noise condition dramatically affects the ability to extract and comprehend information. Unwanted signals and marks on the image are collectively referred to as noise from images, and they frequently contaminate images and provide a hazy impression. Depending on how they impact the image, the noises have different distributions. The noise must be identified based on its pattern and probabilistic properties. Image and signal data include a wide variety of noise [4-6]. Gaussian, Salt & Pepper, Poisson, impulse, and Speckle noise are the most common types of noise that distort images. Effective image denoising is essential in the majority of image processing applications since the performance of subsequent image processing operations completely depends on how well the noise reduction process performs. However, this is a challenging task because the denoising operator must effectively remove

* **Corresponding Author**
*(akif@erciyes.edu.tr) ORCID ID 0000-0001-5164-375X
(ebesdok@erciyes.edu.tr) ORCID ID 0000-0001-9309-375X

Cite this article
Günen, M. A., Beşdok, E. (2023). Effect of denoising methods for hyperspectral images classification: DnCNN, NGM, CSF, BM3D and Wiener. Mersin Photogrammetry Journal, 5(1), 1-9

noise while preserving crucial information in the image. The majority of contemporary filtering algorithms employ sequential statistical filters that make use of the rank information of a sufficient collection of noisy input pixels [7]. Non-local means algorithm (NLM) [8], block matching and 3D filtering algorithm (BM3D) [9], residual learning of deep CNN for image denoising (DnCNN) [3], K-SVD algorithm [10], Markov random field models (MRF) [11], Non-Local Meets Global (NGM) [12], weighted nuclear norm minimization (WNNM) [13], Wiener [14], and a cascade of shrinkage field (CSF) [15] are some of the HSI noise removal approaches that have been presented in recent years.

Due to all of these factors, it is crucial to identify the denoising filter that is appropriate for each type of noise, making this study crucial. This study used the k-nearest neighbor approach to classify Gaussian, Salt & Pepper, Poisson, and Speckled HSI images after applying the DnCNN, NGM, CSF, BM3D, and Wiener filters. The effectiveness of the filtering techniques was compared.

The remainder of this work is structured as follows: Section 2 defines the material and method, Section 3 presents the results and discussion, and Section 4 includes the conclusion.

2. Material

In this study, various types of noise were added to the HSI and then the classification performance of the HSI was investigated by applying some noise removal methods. In this context, the flow chart of the study performed in Figure 1 is presented.

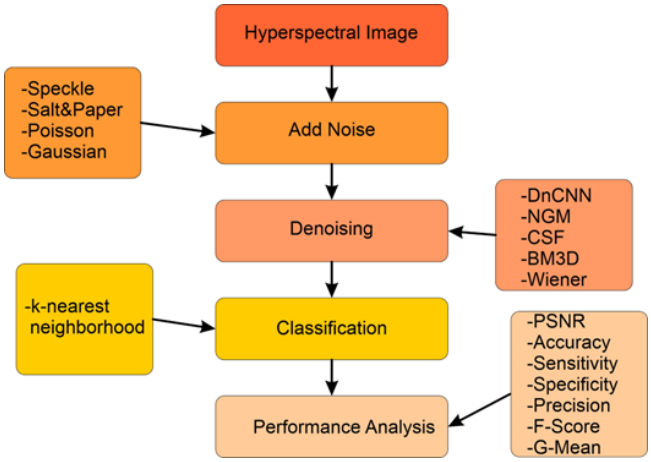

Figure 1. Flow chart of study

Pavia is a dataset acquired using the ROSIS sensor with a ground sampling distance of 1,3 m over the Italian city of Pavia. The dataset is divided into two parts: University of Pavia consist of 103 bands with 610x340 pixels and Pavia Center consist of 102 bands with 1096x715 pixels [16]. In Figure 2, RGB, ground truth and data cube representations of the Pavia University dataset are given.

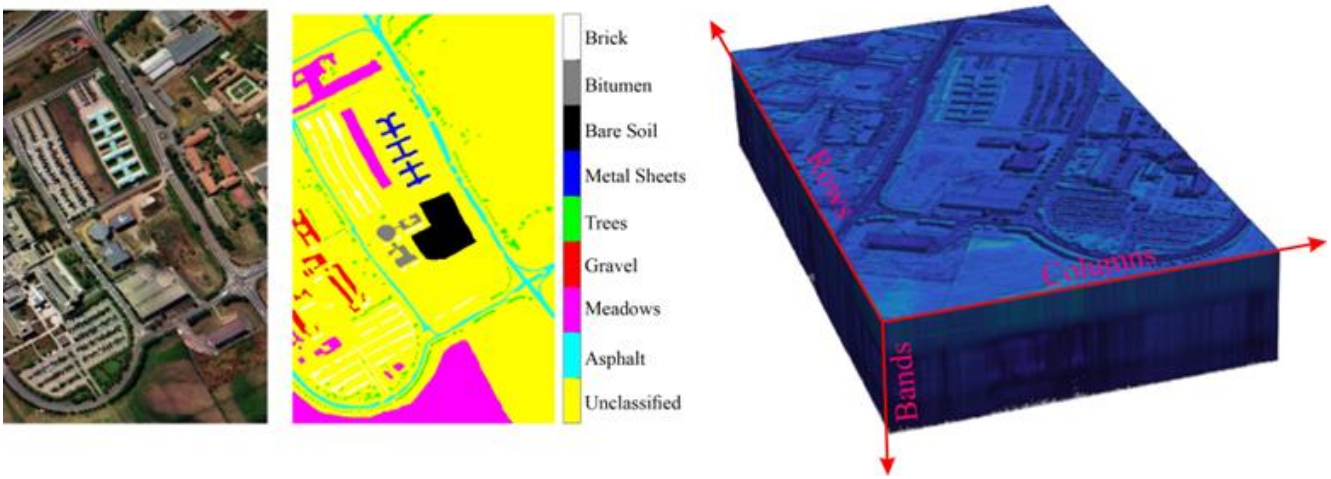

Figure 2. A representation of the RGB, ground truth, and hyperspectral data cube of Pavia HIS

There are various urban elements in Pavia (such metals, bricks, and asphalt etc.). Nine different areas of interest were recognized, making up 50% of the surface. Due to its dimension and ability to assess the usage of HSI for possible applications, this dataset has long been regarded as one of the primary references. Preprocessing may be essential to eliminate some pixels that lack spectral information. The class distribution of the Pavia University data set used in this study is presented in Table 1.

The implementation was carried out using MATLAB 2022a software on a laptop with AMD Ryzen 9 5900HX Radeon 3.30 GHz processor, 32 Gb RAM and AMD Radeon RX 6700M graphics card.

Table 1. Pavia dataset specifications

#	Class Name	Ground Sample
1	Asphalt	6631
2	Meadow	18649
3	Gravel	2099
4	Trees	3064
5	Painted Metal Sheet	1345
6	Bare Soil	5029
7	Bitumen	1330
8	Self-Blocking Brick	3682
9	Shadow	947

3. Methods

In this section, noise types, denoising methods and classification method (i.e., k-nearest neighbor), which form the basis of the proposed method, are explained.

3.1. Noise types

Noise is commonly defined in digital images as a random change in brightness or color information, and it is frequently generated randomly or systematically by the technological constraints of the image acquisition sensor and improper ambient conditions. Furthermore, noise may penetrate the image in a variety of ways during image collecting and transmission. Noise in an image can be either additive or multiplicative. An additional noise signal is added to the original image in the additive noise model to produce a distorted noise image/signal. The original image is multiplied by noise in the multiplicative noise model, but in the additive noise model, the noise is added to the original image to create a distorted noisy image or signal [17-19]. In general, this process can be described as Equation 1.

$$f(x, y) = a(x, y) + b(x, y) \text{ or } f(x, y) = a(x, y) \times b(x, y) \quad (1)$$

(x, y) represents the pixel position, $a(x, y)$ represents the original image, the noise inside the distorted/noise, $b(x, y)$, added image is represented by $f(x, y)$.

Gaussian noises, in which the statistical behavior of random variables is characterized by a probability density function, are typically induced by insufficient illumination conditions, atom thermal vibration, and the discontinuous nature of warm object radiation. Gaussian noise is distributed uniformly throughout the signal. A noisy image is a set of pixels formed by adding the original pixel values to a random Gaussian noise value. A Gaussian's probability distribution function has the shape of a bell. The most typical application for Gaussian noise is white Gaussian noise. The magnitude of the Gaussian Noise rises proportionally to the standard deviation (σ). Salt & pepper noise, also known as impulse noise, appears as black and white dots in the digital image. This model, also referred to as data drop noise, statistically reduces the original data values. Only a few pixels are extremely noisy and are thus generated by dust particles from overheated components in the image acquisition source. This noise occurs in the image as a result of sharp and rapid oscillations in the image signal, and only those few pixels are extremely noisy. Poisson noise appears due to the stochastic nature of electromagnetic waves, including visible light, gamma rays, and x-rays. The non-linear response of image sensors and recorders generates Poisson noise. The image-related term is considered to have its standard deviation because the mean and variance of a Poisson distribution are the same, assuming the variance of the noise is one. Speckle noise, unlike other types of noise, is multiplicative noise. It degrades image quality by simulating a backscattered wave created by diffuse reflection. This form of noise is commonly found in synthetic aperture radar images used in remote sensing investigations, making it difficult for practitioners to detect minute features [20-23].

3.2. Denoising methods

The problem of noisy data, which is often unavoidable in real-world applications, has become a widespread issue that must be addressed with appropriate denoising techniques [24]. Denoising an image is a complex procedure since noise is dependent on the image's high-frequency content. In general, the objective is to achieve a compromise between suppressing noise as much as feasible while losing as little information as possible. Image noise can be removed using filter-based methods such as mean, median, wavelet, or Wiener. Modern approaches, however, have begun to be employed more frequently as computer technology has gained access to high hardware capabilities. Modern approaches such as Deep CNN Residual Learning (DnCNN), Non-local Meets Global (NGM), a cascade of shrinkage fields (CSF), block-matching and 3-D filtering (BM3D), and Wiener methods were used in this study to denoising.

Deep neural networks have made various attempts to address the denoising issue. CNN have recently demonstrated outstanding effectiveness in handling a variety of vision tasks, largely because to the ease of access to large-scale datasets and the advancements in deep learning techniques. DnCNN, a model that has been proposed to handle a variety of low-level tasks, not only resolves issues with image denoising, JPEG block removal, and super resolution, but it also carries out a blind reconstruction without knowing anything about the input image. The VGG network is used by DnCNN to construct the network architecture. 400 images are used to train a network and it is claimed that the residual image is easier to learn than the noisy image. The used DnCNN network has 59 layers. The residual learning formulation is used in the DnCNN model. In contrast to the residual network, which makes utilization numerous residual units, DnCNN only uses one residual unit to estimate the residual image. Additionally, DnCNN's incorporation of batch normalization and residual learning can lead to quick and consistent training as well as improved denoising performance [3]. The MATLAB code for DnCNN can be found at https://github.com/cszn/DnCNN.

The NGM approach [25] was developed for HSI denoising. In order to combine spatial nonlocal similarity and global spectral low-order feature in NGM, the complex HSI denoising paradigm is implemented. From the noisy HSI, first the low-dimensional orthogonal base and its associated reduced image are learned, and then the reduced image and orthogonal base are updated by spatial nonlocal noise removal and recursion regularization, respectively. MATLAB code is available at https://github.com/quanmingyao/NGMeet.

In the CSF method, shrinkage fields, an image restoration architecture derived from existing

optimization algorithms for common random field models, are introduced and combined the random field based model and the unfolded quasi-quadratic optimization algorithm in a single learning framework [15]. The MATLAB code for CSF can be found at https://github.com/uschmidt83/shrinkage-fields.

BM3D proposed by Dabov et al., [26] proposes new image noise removal strategy based on improved sparse representation in the transform domain, and in BM3D, non-local similar patches are adaptively searched twice in a local widow of size 25x25, and thus the final effective patch size is 49x49. Increasing sparsity is accomplished by combining related 2D image segments into 3D data arrays known as groups. BM3D's MATLAB code may be found at https://webpages.tuni.fi/foi/GCF-BM3D/.

There are several classic strategies, but the most basic approach, the Wiener filter, is a linear estimator that minimizes the mean square error between the original and noisy data. It is defined in various ways and utilized in diverse situations. When using a low-pass filter to blur an image, reverse filtering can be used to restore the image. The Wiener filter, developed by Norbert Wiener in 1940, reduces extra noise by conducting an efficient trade-off between reverse filtering and noise smoothing. However, because reverse filtering is particularly sensitive to extra noise, Wiener filtering reverses blur at the same time [24, 27].

3.3. k-nearest neighbor method

One of the most widely used supervised classification methods is the k-nearest neighbor method. Cover and Hart's technique essentially uses k-nearest neighbor pixels for classification [28]. The query pixel is assigned to the class where the predominance is close after first determining the k-nearest neighborhood and measuring the query sample's distance from the training data using distance functions like Cosine, Euclidean, Manhattan, or Minkowski. The training process for the k-closest approach is carried out using training data. The approach makes selecting the best k value rather difficult [29].

4. Results and Discussion

In this study, gaussian, Salt & Pepper, Poisson and Speckle noises were added to the Pavia University dataset. Then, DnCNN, NGM, CSF, BM3D and Wiener denoising methods were applied to the contaminated images and the results were compared statistically. RGB images with noise added are presented in Figure 3.

Figure 3. RGB image of HSI with noise added a) Speckle, b) Salt & Pepper, c) Poisson and d) Gaussian

While performing the noise addition, $\sigma^2 = 0.01$ for Gaussian noise, $d = 0.02$ for Salt & Pepper noise, $\mu = 10$ for Poisson noise and $\sigma^2 = 0.1$ for Speckle noise. The RGB images of the HSIs in which the denoising process is applied after the noise addition are presented in Figure 4. After denoising, the HSI was classified using the k-nearest neighbor method. Before classification, the data set was randomly divided into 30% test and 70% training dataset. A Support Vector Machine could also be used for classification, but due to the dimensionality problem, these algorithms require a lot of workload equipment. In their study, Singh et al., [30] showed that the k-nearest neighbor method provides the most accurate result after support vector machines in HSI classification. Experimental application was carried out using the parameters used in [30]. In this context, cosine distance functions, 10 nearest neighbor number (k) and equal distance weight parameters are preferred. When looking at Figure 4, it is clear that the impacts of Gaussian noise on RGB cannot be totally avoided, particularly for BM3D and Wiener. Furthermore, the influence of salt & pepper noise cannot be seen removed for DnCNN and Wiener. The CSF approach resulted in texture softening, particularly in structures with sharp corners and areas of land type change. By changing the density difference of objects with varying reflectance values, the NGM approach has made it more visible.

In terms of noise types, BM3D, an effective and powerful extension of the non-local averaging method, generated extremely consistent findings. BM3D is a two-stage, non-local filtering approach in transform space in which related patches are stacked in 3D groups and then transformed into wavelet space using block mapping. The wavelet domain is then used for coefficient Wiener filtering. Because peak-signal-to-noise ratio (PSNR) does not always guarantee an improvement in the visual effect, Figure 5 shows an overlay of the denoised and classified with k-nearest neighbor of HSI on the RGB image.

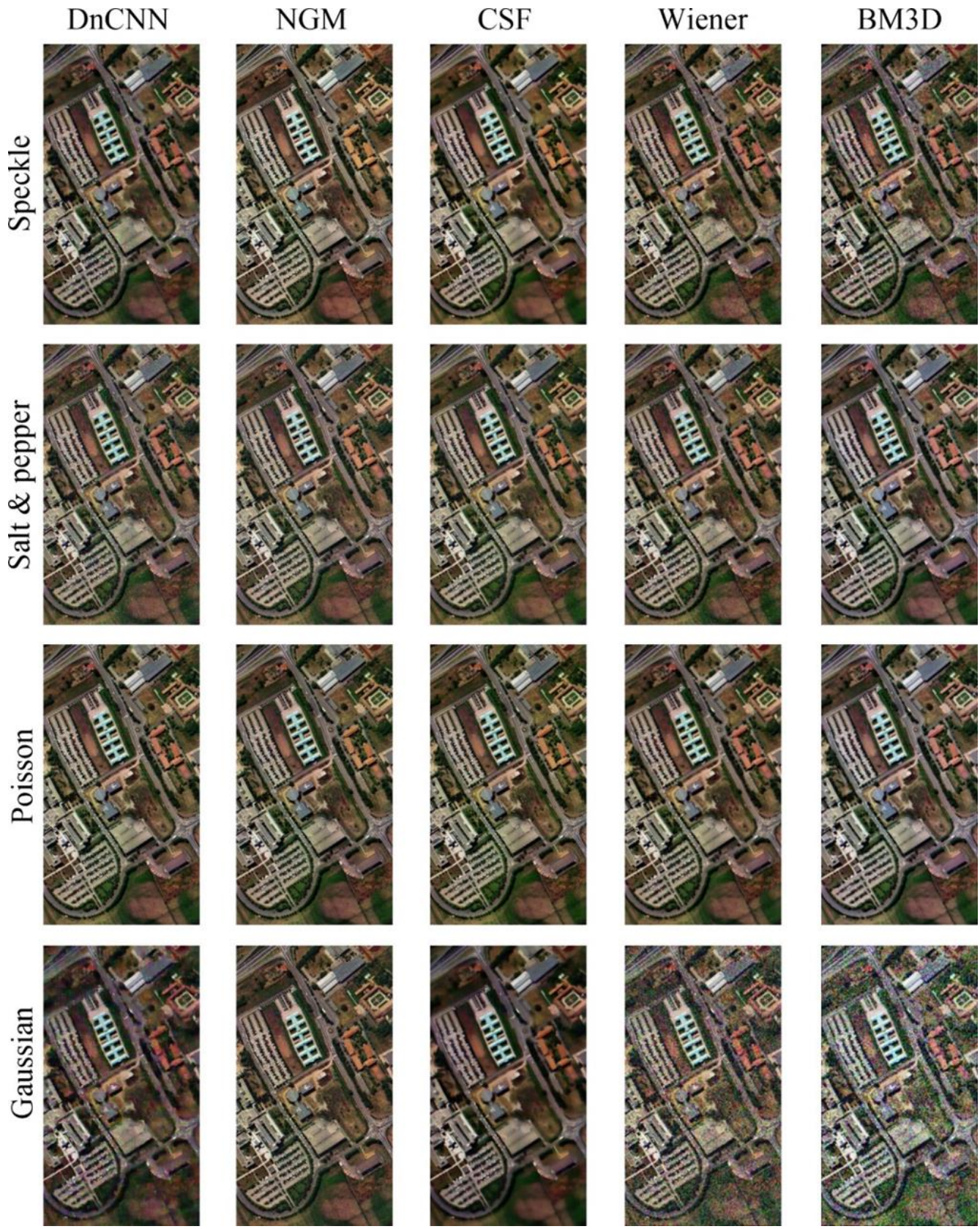

Figure 4. Denoising results of HSI exposed to various sources of noise

Many analyses were carried out using the ground truth data from the classified images. Figure 6 shows the PSNR results of denoising based on ground truth data. In statistical comparisons, the accuracy metric alone does not yield useful conclusions. The distribution of the data sets in Table 1 shows that the meadow areas have more samples than the shadow areas. The usage of various metrics in unbalanced data sets is required as a result.

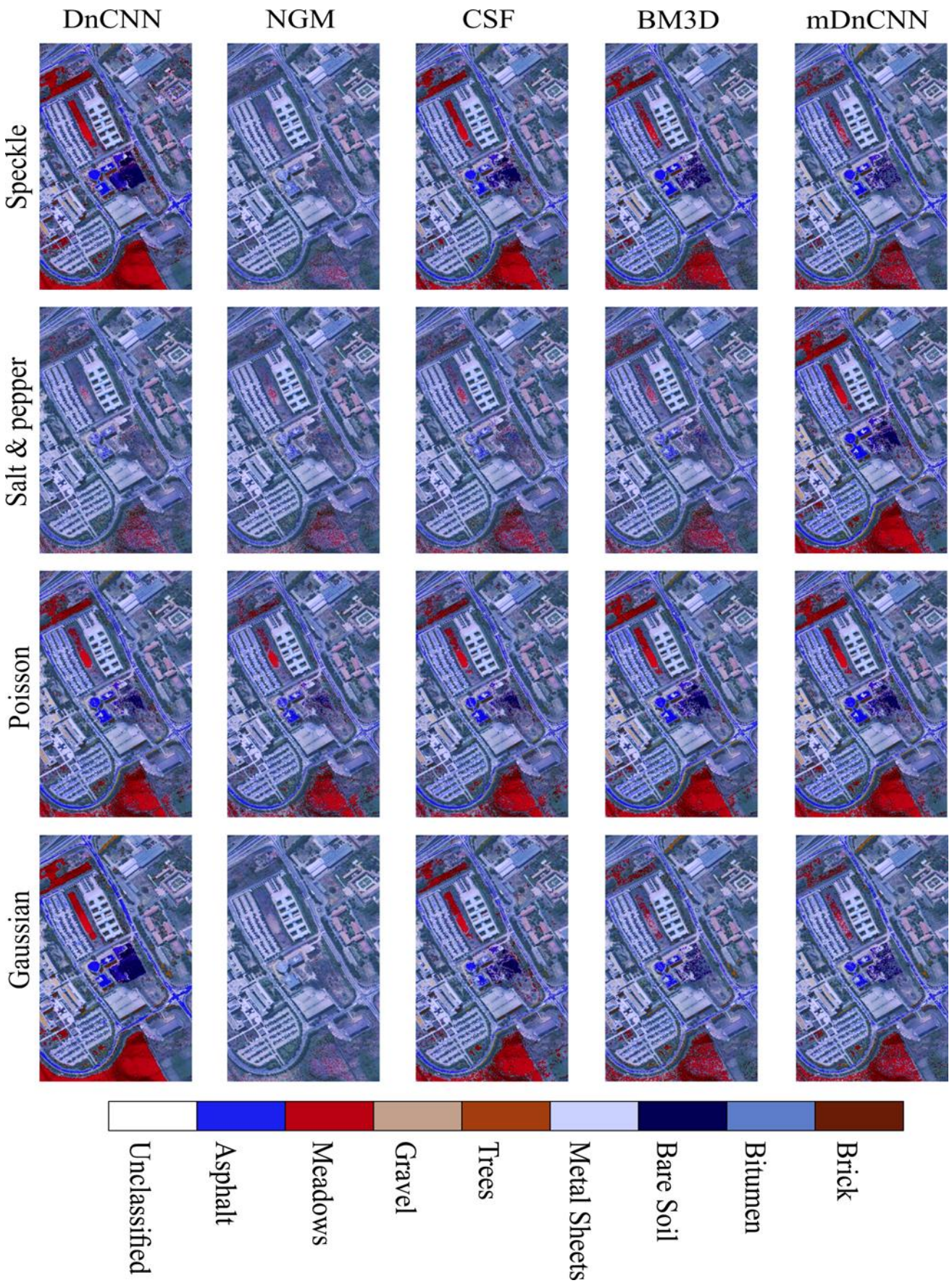

Figure 5. Overlaid classification results on RGB image

The performance of five distinct denoising filters (i.e., DnCNN, NGM, CSF, Wiener, and BM3D) was compared for four different types of noise (i.e., Speckle, Salt & Pepper, Poisson, and Gaussian) in the following Table 2. For each filter, the six-performance metrics -accuracy, sensitivity, specificity, precision, F-Score, and G-Mean- were calculated. With Salt & Pepper noise, the accuracy metrics obtained by Wiener and NGM are reasonably comparable, however the specificity and G-mean values demonstrate that the methods produce different results.

The fact that NGM produces the worst result especially for the Salt & Pepper method shows that the method is ineffective against this noise. NGM produces more effective sensitivity results for Poisson noise than other types of noise. In general, approaches other than the BM3D method could not produce very effective results with Salt & Pepper noise, while all methods could effectively produce results with Poisson noise.

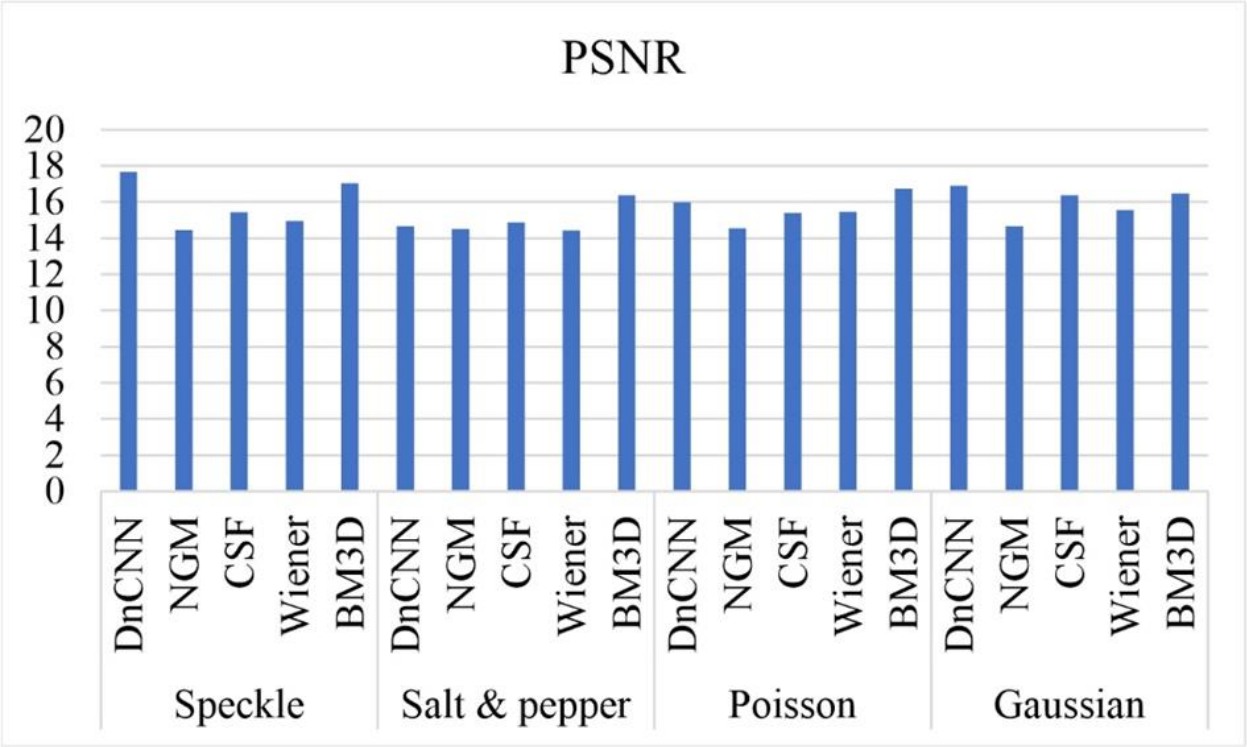

Figure 6. PSNR value based on the Pavia dataset

Table 2. Statistical results calculated according to the Pavia dataset (*Bold marked indicated best result)

		Accuracy	Sensitivity	Specificity	Precision	F-Score	G-Mean
Speckle	DnCNN	**93.20**	96.68	**78.70**	**94.84**	**95.75**	**87.88**
	NGM	79.74	96.76	14.15	81.33	88.37	36.16
	CSF	85.20	93.78	50.05	88.34	90.98	69.70
	Wiener	85.45	90.94	55.14	90.79	90.86	76.33
	BM3D	89.35	**98.39**	62.06	89.27	93.61	73.35
Salt & Pepper	DnCNN	80.16	**98.99**	10.43	80.48	88.78	28.22
	NGM	79.25	96.85	10.62	80.86	88.14	32.23
	CSF	81.93	94.49	33.12	84.60	89.27	55.87
	Wiener	79.00	97.30	7.21	80.41	88.06	27.40
	BM3D	**88.62**	93.57	**64.59**	**92.19**	**92.88**	**80.74**
Poisson	DnCNN	87.53	96.06	57.27	89.07	92.43	72.59
	NGM	79.94	**96.31**	16.85	81.73	88.42	39.49
	CSF	84.30	94.08	45.48	87.20	90.51	65.93
	Wiener	86.08	94.84	52.22	88.49	91.55	70.20
	BM3D	**89.47**	94.93	**66.43**	**92.04**	**93.46**	**80.67**
Gaussian	DnCNN	**89.75**	**98.65**	**63.51**	89.5	**93.85**	**74.11**
	NGM	80.83	96.07	22.93	82.65	88.86	45.42
	CSF	88.30	94.16	62.36	**91.39**	92.76	78.51
	Wiener	86.00	95.70	50.51	87.80	91.58	67.95
	BM3D	88.05	98.17	56.60	88.12	92.87	69.57

It is an important result that DnCNN produces effective results in Speckle noise as well as Gaussian. By learning the residual noise rather than the denoised image directly, researchers suggested [3] to denoise natural images using additive Gaussian noise using DnCNN. Similar research has been used as the foundation for various image processing networks, including Speckle de-noising [31] and the detection of illness in tomato leaves [32]. However, the disadvantage of vanishing gradients, which can happen with very deep networks, is reduced via residual learning. In contrast to other methods, NGM performs well just in the sensitivity criterion and poorly in the other criteria. This suggests that NGM is not the ideal choice for various sorts of noise. While the CSF method shows lower performance in sensitivity and specificity criteria compared to other

methods, it shows high performance against other criteria. This indicates that CSF may give less accurate results than other methods. The Wiener technique performs moderately in all noise types; however, it performs poorly by the G-mean criterion when compared to other methods. This indicates that, in many situations, the Wiener technique tends to produce less reliable result than other methods.

5. Conclusion

Denoising in multidimensional images has recently grown in popularity as a study area with potentially significant applications. This paper discusses the issue of denoising in high-dimensional remote sensing images and evaluates the effectiveness of five distinct approaches. Four additional noises have been added in this situation, and HSI has been classified. Denoising performance can be defined by high benchmarks. Looking at the quantitative and qualitative results, the BM3D filter generally outperformed other filters. In particular, the BM3D filter for Salt & Pepper and Gaussian noise had the highest G-Mean, with a higher accuracy, sensitivity, specificity, precision, and F-Score than the other filters. Denoising techniques performed better against Poisson noise even though they were statistically ineffective against Salt & Pepper noise. The DnCNN filter performed better than other filters for Gaussian and Salt & Pepper noises, but failed for Poisson and Speckle noises. NGM and Wiener filters performed the worst for all noise types. The low specificity of the NGM filter and the low sensitivity of the Wiener filter are particularly notable. As a result, evaluating the performance of different denoising filters for different noise types aids in determining the optimum filter for a given application. In summary, this study highlights the importance of selecting an appropriate denoising method for hyperspectral images to improve their quality and usability for land use/cover analysis. The results suggest that DnCNN and BM3D are the most effective methods for denoising hyperspectral images, while the CSF, Wiener, and NGM approaches have limitations and may not be suitable for certain noise types.

The main advantage of this research is the comparison of a diverse variety of HSI noise reduction techniques to identify the most successful approach. The performance of various approaches has been evaluated using a variety of situations and criteria. The disadvantage of working with HSI data is that processing the data is difficult because of the enormous amount of data dimensionality, the requirement for a big data set, and the requirement to select parameters for the classification technique and filters. For these reasons, methods will be tested on various data sets (such as Salinas A, Indian Pines, and Botswana, etc.) in future studies. The effectiveness of filtering methods according to different data dimensions will also be investigated. Because a thorough investigation is needed to determine how different feature reduction techniques (i.e., Principal component analysis, Linear discriminant analysis, and minimum redundancy maximum relevance etc.) affect the outcome.

Author contributions

Mehmet Akif Günen: Conceptualization, Validation, Visualization, and Investigation **Erkan Beşdok:** Writing, Reviewing and Editing.

Conflicts of interest

The authors declare no conflicts of interest.

References

1. Günen, M. A., Atasever, U. H., & Beşdok, E. (2020). Analyzing the contribution of training algorithms on deep neural networks for hyperspectral image classification. Photogrammetric Engineering & Remote Sensing, 86(9), 581-588.
2. Nofrizal, A. Y., Sonobe, R., Hiroto, Y., Morita, A., & Ikka, T. (2022). Estimating chlorophyll content of Zizania latifolia with hyperspectral data and random forest. International Journal of Engineering and Geosciences, 7(3), 221-228.
3. Zhang, K., Zuo, W., Chen, Y., Meng, D., & Zhang, L. (2017). Beyond a gaussian denoiser: Residual learning of deep cnn for image denoising. IEEE transactions on image processing, 26(7), 3142-3155.
4. Lam, A., Sato, I., & Sato, Y. (2012, November). Denoising hyperspectral images using spectral domain statistics. In Proceedings of the 21st International Conference on Pattern Recognition (ICPR2012) (pp. 477-480). IEEE.
5. Annam, S., & Singla, A. (2020, November). Correlative analysis of denoising methods in spectral images embedded with different noises. In 2020 Sixth International Conference on Parallel, Distributed and Grid Computing (PDGC) (pp. 318-323). IEEE.
6. Momeny, M., Jahanbakhshi, A., Neshat, A. A., Hadipour-Rokni, R., Zhang, Y. D., & Ampatzidis, Y. (2022). Detection of citrus black spot disease and ripeness level in orange fruit using learning-to-augment incorporated deep networks. Ecological Informatics, 71, 101829.
7. Yuksel, M. E., & Besdok, E. (2004). A simple neuro-fuzzy impulse detector for efficient blur reduction of impulse noise removal operators for digital images. IEEE Transactions on Fuzzy Systems, 12(6), 854-865.
8. Buades, A., Coll, B., & Morel, J. M. (2005, June). A non-local algorithm for image denoising. In 2005 IEEE computer society conference on computer vision and pattern recognition (CVPR'05) (Vol. 2, pp. 60-65). IEEE.
9. Dabov, K., Foi, A., Katkovnik, V., & Egiazarian, K. (2006, February). Image denoising with block-matching and 3D filtering. In Image processing: algorithms and systems, neural networks, and machine learning (Vol. 6064, pp. 354-365). SPIE.
10. Aharon, M., Elad, M., & Bruckstein, A. (2006). K-SVD: An algorithm for designing overcomplete dictionaries for sparse representation. IEEE Transactions on signal processing, 54(11), 4311-4322.
11. Li, S. Z. (2009). Markov random field modeling in image analysis. Springer Science & Business Media.

12. He, W., Yao, Q., Li, C., Yokoya, N., Zhao, Q., Zhang, H., & Zhang, L. (2020). Non-local meets global: An iterative paradigm for hyperspectral image restoration. IEEE Transactions on Pattern Analysis and Machine Intelligence, 44(4), 2089-2107.
13. Gu, S., Zhang, L., Zuo, W., & Feng, X. (2014). Weighted nuclear norm minimization with application to image denoising. In Proceedings of the IEEE conference on computer vision and pattern recognition (pp. 2862-2869).
14. Ghael, S., Sayeed, A. M., & Baraniuk, R. G. (1997, July). Improved wavelet denoising via empirical Wiener filtering. In SPIE Technical Conference on Wavelet Applications in Signal Processing.
15. Schmidt, U., & Roth, S. (2014). Shrinkage fields for effective image restoration. In Proceedings of the IEEE conference on computer vision and pattern recognition (pp. 2774-2781).
16. Günen, M. A., Atasever, U. H., & Beşdok, E. (2020). Analyzing the contribution of training algorithms on deep neural networks for hyperspectral image classification. Photogrammetric Engineering & Remote Sensing, 86(9), 581-588.
17. Yüksel, M. E., Baştürk, A., & Beşdok, E. (2004). Detail-preserving restoration of impulse noise corrupted images by a switching median filter guided by a simple neuro-fuzzy network. EURASIP Journal on Advances in Signal Processing, 2004(16), 1-11.
18. Çivicioğlu, P., Alçı, M., & Beşdok, E. (2004). Impulsive noise suppression from images with the noise exclusive filter. EURASIP Journal on Advances in Signal Processing, 1-7.
19. Beşdok, E. (2004). A new method for impulsive noise suppression from highly distorted images by using Anfis. Engineering Applications of Artificial Intelligence, 17(5), 519-527.
20. Kumar, N., & Nachamai, M. (2017). Noise removal and filtering techniques used in medical images. Oriental Journal of Computer Science & Technology, 10(1), 103-113.
21. Patidar, P., Gupta, M., Srivastava, S., & Nagawat, A. K. (2010). Image de-noising by various filters for different noise. International Journal of Computer Applications, 9(4), 45-50.
22. Kanagalakshmi, K., & Chandra, E. (2011, April). Performance evaluation of filters in noise removal of fingerprint image. In 2011 3rd International Conference on Electronics Computer Technology (Vol. 1, pp. 117-121). IEEE.
23. Niknejad, M., & Figueiredo, M. A. (2018, September). Poisson image denoising using best linear prediction: a post-processing framework. In 2018 26th European Signal Processing Conference (EUSIPCO) (pp. 2230-2234). IEEE.
24. Atasever, U. H., & Gunen, M. A. (2021). Change detection approach for SAR imagery based on arc-tangential difference image and k-Means++. IEEE Geoscience and Remote Sensing Letters, 19, 1-5.
25. He, W., Yao, Q., Li, C., Yokoya, N., & Zhao, Q. (2019). Non-local meets global: An integrated paradigm for hyperspectral denoising. In Proceedings of the IEEE/CVF Conference on Computer Vision and Pattern Recognition (pp. 6868-6877).
26. Dabov, K., Foi, A., Katkovnik, V., & Egiazarian, K. (2007). Image denoising by sparse 3-D transform-domain collaborative filtering. IEEE Transactions on image processing, 16(8), 2080-2095.
27. Juang, L. H., & Wu, M. N. (2010). Image noise reduction using Wiener filtering with pseudo-inverse. Measurement, 43(10), 1649-1655.
28. Cover, T., & Hart, P. (1967). Nearest neighbor pattern classification. IEEE transactions on information theory, 13(1), 21-27.
29. Günen, M. A. (2022). Performance comparison of deep learning and machine learning methods in determining wetland water areas using EuroSAT dataset. Environmental Science and Pollution Research, 29(14), 21092-21106.
30. Singh, S., Singh, D., Sajwan, M., Rathor, V. S., & Garg, D. (2022). Hyperspectral image classification using multiobjective optimization. Multimedia Tools and Applications, 81(18), 25345-25362.
31. Park, D. Y., & Park, J. H. (2020). Hologram conversion for speckle free reconstruction using light field extraction and deep learning. Optics Express, 28(4), 5393-5409.
32. Karthik, R., Hariharan, M., Anand, S., Mathikshara, P., Johnson, A., & Menaka, R. (2020). Attention embedded residual CNN for disease detection in tomato leaves. Applied Soft Computing, 86, 105933.

Mersin Photogrammetry Journal

https://dergipark.org.tr/en/pub/mephoj

e-ISSN 2687-654X

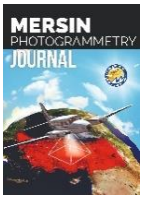

Preserving human privacy in real estate listing applications by deep learning methods

Yunus Emre Varul[1*], Hilal Adıyaman[1], Tolga Bakırman[1], Bülent Bayram[1], Elif Alkan[1], Sevgi Zümra Karaca[1], Raziye Hale Topaloglu[1]

[1]*Yildiz Technical University, Department of Geomatics Engineering, Türkiye*

Keywords
Real Estate
Privacy
Resnet-50
Inceptionv3
DenseNet-169

Research Article
DOI:10.53093/mephoj.1213893

Received:03.12.2022
Revised: 12.01.2023
Accepted:16.01.2023
Published:27.05.2023

Abstract

The images are important components of real estate applications on the internet to inform users. There are multiple rental and sale properties and many images of these properties on the internet, and it is challenging to control the images of these real estate in terms of time, workload, and cost. Considering the requirements of the problem, Deep Learning (DL), one of the Artificial Intelligence (AI) methods, offers ideal solutions. This study aims to distinguish images that contain humans using deep learning techniques. This will also aid in not violating the privacy of people according to the Law on the Protection of Personal Data in the image content used in real estate applications. For this purpose, firstly, a dataset of real estate images with and without humans called the Real Estate Privacy (REP) dataset was created. The REP dataset was split into 70%, 20%, and 10% for training, validation, and testing, respectively. Secondly, the REP dataset was trained with Inceptionv3, ResNet-50, and DenseNet-169 architectures using transfer learning. Lastly, the performances of the architectures were evaluated by accuracy, precision, recall, and F1-score accuracy metrics. Experimental results indicate that the 52 epoch ResNet-50 architecture is the best for our datasets with 98.45% overall accuracy and 98.00% precision, 98.90% recall, and 98.44% F1-score. The Inceptionv3 model provided the best results on the 55th epoch with 98.27% accuracy, 97.81% precision, 98.71% recall, and 98.26% F1-score. Finally, the DenseNet-169 model produced the best results on the 47th epoch, with 97.81% accuracy, 97.09% precision, 98.52% recall, and 97.80% F1-score. Accuracy assessment shows that the highest accuracy among the three architectures was obtained with the ResNet-50 architecture This study shows that deep learning methods offer a perspective to image content control and can be used efficiently in real estate applications.

1. Introduction

Real estate has a physical and psychological impacts on people, depending on its location, accessibility, and constraints, beyond meeting basic needs [1]. In addition to location, accessibility, and constraints, there are many factors for real estate preferences and prices along with the interior and exterior elements such as wall paint and floor materials, many visual details such as the appearance of the neighborhood, the view seen outside, and the condition of the accessories [2].

Nowadays, Internet technologies are extensively used to advertise real estate [3]. Real estate for sale or rent is usually promoted by using images of a property [4]. The images and digital files of real estate are often uploaded to the systems by users over which the publisher has to check the content of the image manually. Unwanted situations due to this uncontrolled content can cause great material and moral damage to publishers. The images that are made available to many users over the internet must be suitable for the listed real estate. to minimize the damage [5].

According to the Law on the Protection of Personal Data, it is expected that the relevant photos must only contain the properties of the real estate [6]. Considering that a large number of real estate images are uploaded to these portals, people can't control the content of images in terms of time and workload. Since there is a large amount of content that human inspection cannot deal with errors and cost constraints, it is possible

* **Corresponding Author**

*(varul.emre@gmail.com) ORCID ID 0000-0001-5827-3712
(hilal.adiyaman@std.yildiz.edu.tr) ORCID ID 0000-0003-0529-9286
(bakirman@yildiz.edu.tr) ORCID ID 0000-0001-7828-9666
(bayram@yildiz.edu.tr) ORCID ID 0000-0002-4248-116X
(elif.alkan1@std.yildiz.edu.tr) ORCID ID 0000-0003-3498-5074
(karacasevgi7@gmail.com) ORCID ID 0000-0001-7301-2166
(haletopaloglu48@gmail.com) ORCID ID 0000-0001-9706-8068

Cite this article

Varul, Y. E., Adıyaman, H., Bakırman, T., Bayram, B., Alkan, E., Karaca, S. Z., & Topaloğlu, R. H. (2023). Preserving human privacy in real estate listing applications by deep learning methods. Mersin Photogrammetry Journal, 5(1), 10-17

to perform this inspection automatically using computer vision and artificial intelligence (AI). Recently, deep learning (DL) which is one of the machine learning (ML) methods, has become popular with the graphics processing units that have been developing and increasing in capacity in the AI field [7,8].

Many DL networks have been proposed for image classification in recent years. After the great success of AlexNet on the ImageNet dataset using Convolutional Neural Networks (CNN), DL approaches have become widespread [9]. The architectures and training procedures still need improvements, as they usually work on a patch-based framework. Long et al. [10] proposed fully convolutional networks (FCNs) that improve CNNs. Simonyan and Zisserman [11] and Szegedy et al. [12] proposed VGG and GoogLeNet (Inception) networks, respectively, showing that deeper and wider networks provide increased accuracy. He et al. [13] then presented the ResNet framework, where layers are formulated by learning residual functions concerning layer inputs. The ResNeXt network developed by Xie et al. [14] is built by repeating a building block that combines a series of transformations with the same topology. The main strategy of ResNeXt is "divide-transform-merge", similar to an Inception module. Huang et al. [15] proposed the DenseNet network, which connects each layer to all other layers in a feed-forward manner, with the approach that a more accurate and efficient training process can be realized by having shorter connections between the layers close to the input and the layers close to the output. Zoph et al. [16] proposed the NASNet network that learns model architectures directly on the dataset of interest. The EfficientNet network developed by Tan and Le [17] proposes a new scale-up method called compound scaling to achieve higher accuracy.

Various image classification techniques have been used for diverse aims in the field of property in real estate agencies. Bappy et al. [3] used long-short-term memory (LSTM) and fully connected neural networks to classify real estate photos according to room types. Koch et al. [18] tested a multi-scale pattern extraction method for the automatic detection of the current condition of a real estate property. Zeppelzauer et al. [19] proposed a two-step approach for real estate age detection. Zhao et al. [20] integrated deep learning and XGBoost methods for automatic real estate valuation with unstructured data. Kamara et al. [21] proposed a hybrid artificial neural network consisting of convolutional neural networks and bidirectional LSTM to predict the advertisement time of real estate in the passive market.

As can be seen from the literature, no study deals with the content of real estate images in terms of protecting people's privacy. The main aim of this study is to conduct human control in image contents used in real estate applications with deep learning techniques. For this purpose, a dataset called Real Estate Privacy (REP) was created using real estate images with and without humans. This dataset was used for the training of deep learning networks named InceptionV3, Deep Residual Network (ResNet-50), and Densely Connected Convolutional Network (DenseNet-169) architectures.

2. Dataset

The REP prepared within the scope of the study is composed of images with and without humans and various factors such as the resolution of the images, the type of human figure, its clarity (blurring ratio), the brightness and tonality of the environment were taken as a basis in the creation of the data set. 495 human-free images were obtained from the real estate images of the project industry advisor the Gayrimenkul Borsası A.Ş. (GABORAS) 2552 human-free images were included in the study from the ADE20K dataset, which consists of 20 thousand scene-centered images in 150 object categories offered as open source [22]. Figure 1 shows examples of image samples from GABORAS Gayrimenkul Borsası A.Ş and ADE20K used in the study.

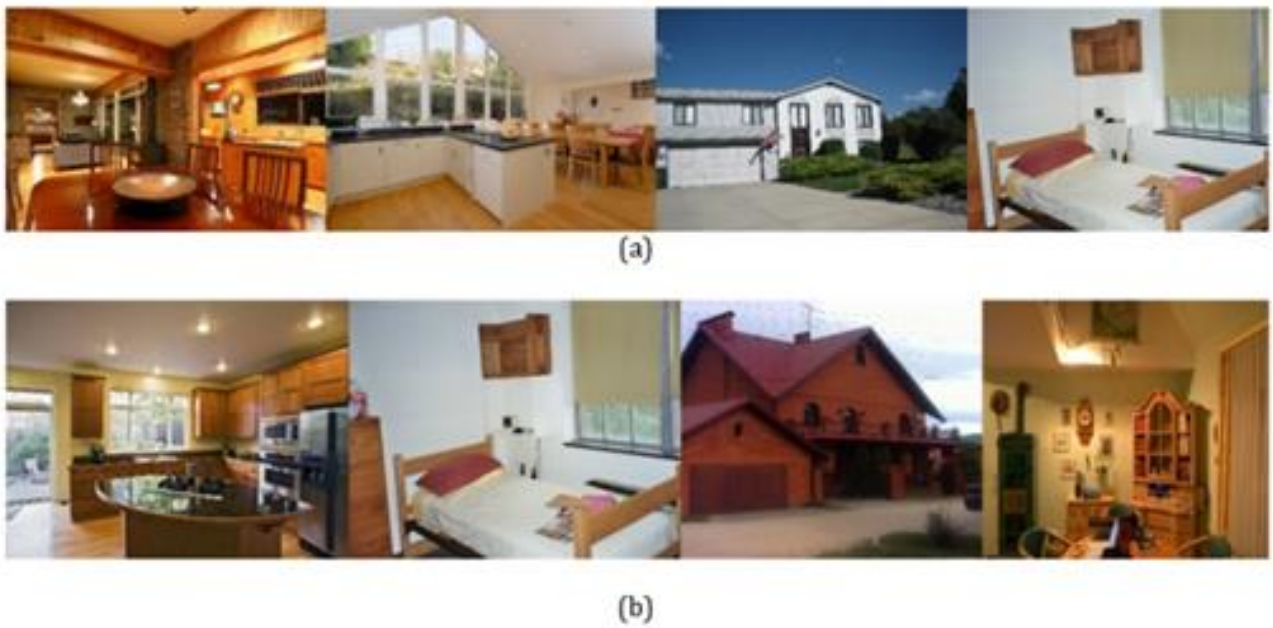

Figure 1. (a) Sample property images of GABORAS Gayrimenkul Borsası A.Ş., (b) Sample images of ADE20K data set

Furthermore, new images from videos of home trips, tours, etc. published on social media platforms were included in the study dataset to complete the missing data. The images were obtained by extracting frames from the videos every 3 second, however, blurring was detected in some frames due to the motion within the videos. For this reason, the average blur rates of each video were calculated. Frames with values greater than the rates were not included in the dataset. The operations were performed using the OpenCV library in a Python environment. Images with different types of people and environments were manually selected to avoid possible overfitting in deep learning algorithms. As a result, 19065 images with people and 2225 images without people were obtained. Images collected from social media platforms are given in Figure 2. The content of the REP data set is shown in Table 1.

19065 images with people and 5272 images without people in different resolutions were obtained. If these images that equal to or larger than 512x512, they were resized as 512x512. However, 5272 images were used for homogeneous data distribution in both classes.

The REP data set was separated into Training, Validation, and Test data for use in DL architectures. 70%, 20%, and %10 of the dataset is reserved for training, validation, and testing, respectively. The number of training data is shown in Table 2.

Figure 2. (a) Images containing human figures, (b) images without human figures obtained from social media platforms

Table 1. REP dataset content

Class	ADE20K	Gaboras	Social media platforms	Total
Manned	-	-	19065	19065
Unmanned	2552	495	2225	5272

Table 2. Distribution of training data

Class	Train	Validation	Test	Total
Manned	3690	1054	528	5272
Unmanned	3690	1054	528	5272

3. Methodology

AI is a technology that can be created by intelligent systems that can imitate human intelligence. ML is one of the important methods to achieve AI, has enabled machines to learn from past data or experiences without programming. The most popular machine learning technique in recent years has become DL which has provided fast, reliable, and practical solutions using artificial neural networks [23]. DL is one of the rapidly developing methods in big data analytics and has been described as a milestone technology [24].

As can be seen in the literature, many DL networks have been proposed in image classification over time. In this study, Inceptionv3, ResNet, and DenseNet networks are utilized since they are accepted as reference methods in many studies and they achieved great success in the ImageNet dataset. Figure 3 summarizes the whole flow chart of this research.

3.1. ResNet

The ResNet [25] network provides a residual learning framework to facilitate the training of significantly deeper networks. ResNet learns residual functions based on layer inputs Instead of learning reference-free functions. Rather than fitting every few chunk layers directly to the desired base mapping, residual networks allow these layers to fit a residual mapping.

They stack the residual blocks on top of each other to form a network. ResNet-50 has fifty layers using these blocks. Experiments on the ImageNet dataset have shown that residual networks are easier to optimize and can gain accuracy from significantly increased depth [7].

There are three variants of the ResNet network such as ResNet-50, ResNet-101, and ResNet-152, which are frequently used with increasing depths with an increasing number of blocks [26].

Figure 3. The whole flow chart of this research

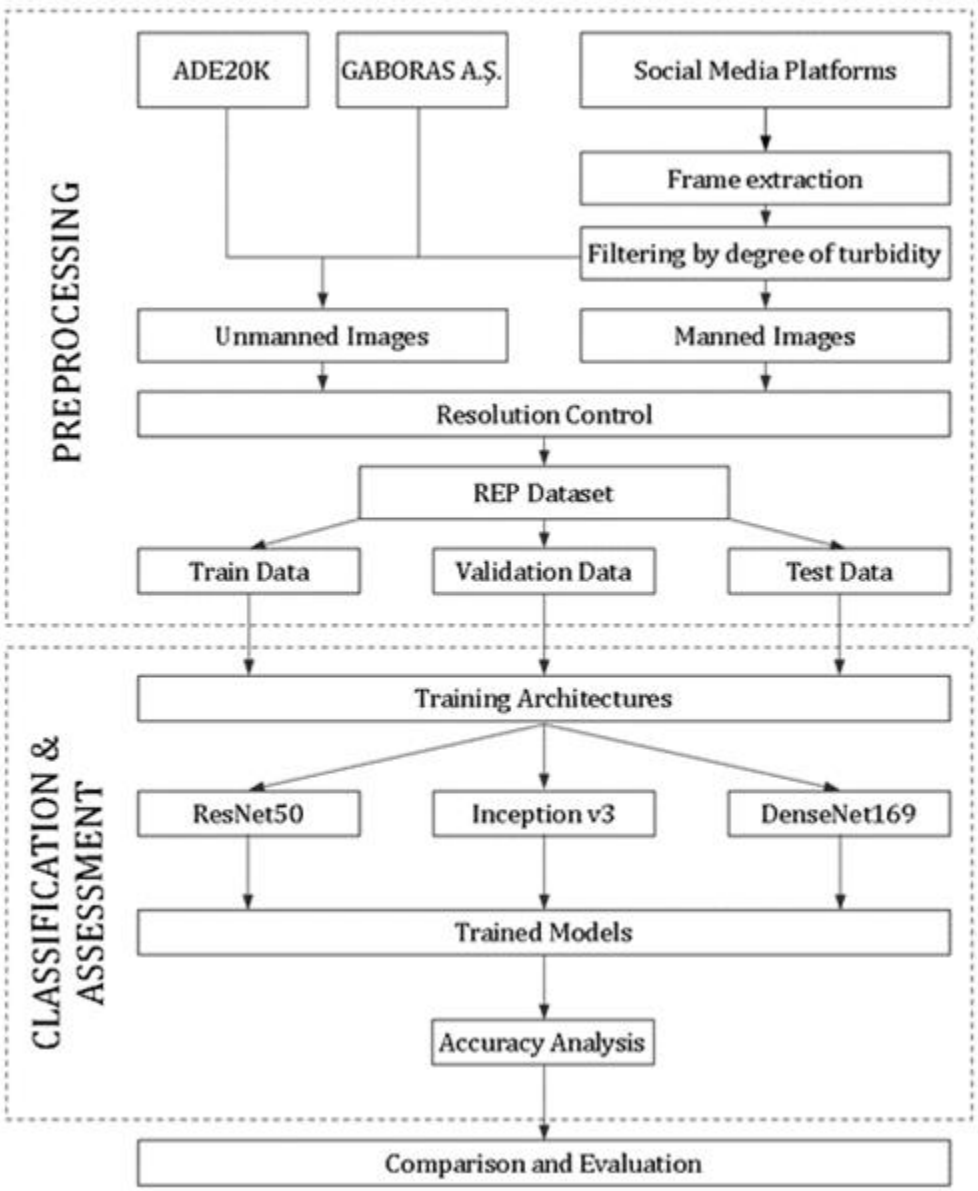

3.2. Inceptionv3

Inceptionv3 network is constructed in a step-by-step progressive manner [27,28]. As a first step, convolutions are factored in to reduce the number of parameters in the network, which helps computational efficiency and controls network efficiency. For this purpose, convolutions are factorized in a smaller size and asymmetrically. Secondly, the CNN is added as an auxiliary classifier between the layers during training [29]. While in previous versions of Inception, this was used to create a deeper network, it is used as a regularizer in Inceptionv3. As a final step, the activation plane of the network filters is expanded to avoid the computational bottleneck caused by the pooling process often used in traditional applications. In this way, an effective grid size reduction method is used to design a low computational load and efficient network [30].

3.3. DenseNet

Dense Convolutional Network (DenseNet) was inspired by the Resnet architecture, which aims to eliminate the information loss that occurs as the depth of the networks increases in traditional Convolutional Neural Networks (CNNs) approaches [15]. DenseNet is proposed as a CNNs-based network in which all layers are feed-forward connected to all other layers. Layers receive inputs from each preceding layer and transmit feature maps to the next layers, maintaining the feed-

forward structure. Unlike the ResNet architecture's method of transferring them to other layers by collecting features, the features are combined and transferred to the next layers in DenseNet. Since the dense connection model does not relearn unnecessary feature maps, the number of parameters is reduced [31]. Narrow layers add small feature maps to the total information of the network. Classification is performed by deciding on all feature maps in the network. The blocks where the dense connection principle is used include convolution and pooling layers. DenseNet also has versions consisting of 121, 169, 201, and 269 layers. In DenseNet architectures, a 0.2 dropout rate is applied after each convolution layer in all convolution layers except the first. In addition to this, the ReLU activation function is used following the convolution layers [26].

It is aimed to classify images with or without human figures at various angles and indoor-outdoor conditions by using the mentioned deep learning architectures. Table 3 is shown the software and hardware specifications and Table 4 illustrates the used hyperparameters.

Table 3. Used hardware and software

Computer	TUBITAK ULAKBIM High Performance and Grid Computing Centre
CPU	Xeon 6148 2.40GHz - 20 cores x 2 CPU
GPU	4xNvidia V100 GPU
SPECfp_rate_base2006	1400
Theoric Gflops	2048Gflops & 4x7800Gflops
Memory	384 GB & 4x16 GB HBM
Definition	Akya-Cuda Cluster

Table 4. Used hyper-parameters

Models	Resnet50, Inception v3, DenseNet169
Library	Tensorflow, Keras
Learning Rate	0.001
Pooling	average
Optimizer	Adam
Activation Function	SoftMAX
Loss Function	Categorical Cross Entropy
Epoch	100

4. Results and Discussion

In this study, the performance of 3 DL architectures namely ResNet50, DenseNet169, and Inceptionv3 is investigated. Python's Keras library was utilized to implement all of the selected deep CNN architectures [32]. 70% of the dataset was used for training, 20% for validation, and 10% for testing. The training, validation, and test data consists of 3840 images, 1098 images, and 549 manned and unmanned images respectively. Furthermore, trainings were performed to find the combination that obtains the best accuracy result with the ideal hyperparameters in DL architectures. In this part, firstly the best epoch of each training was identified and then the accuracy was analyzed on the test data, finally, the hyperparameter combinations were compared. According to the results, the best combination was determined as the pooling method "Average", the optimization method "Adam", the activation function "Softmax" and the loss function "Categorical Cross Entropy".

In addition, accuracy, precision, recall, and F1-Score metrics were used to analyze the results. Table 5 illustrates the accuracy assessment results. The Resnet-50 architecture obtained a high level of success in all evaluation criteria for test accuracy, precision, recall, and F1-Score. The test accuracy, average precision, average call, and F1-score results were calculated as 98.45%, 98.00%, 98.90%, and 98.44%, respectively.

Table 5. Accuracy assessment results for the REP dataset

Deep Learning Model Used	Test Accuracy (%)	Precision (%)	Recall (%)	F1-Score (%)
ResNet-50 (Epoch 52)	98.45	98.00	98.90	98.44
Inceptionv3 (Epoch 55)	98.27	97.81	98.71	98.26
DenseNet (Epoch 47)	97.81	97.09	98.52	97.80

Table 6. Confusion matrix from three architecture

Architecture	Classification Data	Reference Data	
		Manned	Unmanned
ResNet-50	Manned	538	11
	Unmanned	6	543
Inceptionv3	Manned	537	12
	Unmanned	7	542
DenseNet-169	Manned	533	16
	Unmanned	8	541

The confusion matrix shows the relationships between the test classes as a result of the prediction of the data whose real classes were known. The matrix results for the best epochs of the experiments with Resnet-50, Densenet-169, and Inceptionv3 models are given in Table 6.

The observations on confusion matrices show that Densenet-169 was the model with the most misclassifications. Although the Inceptionv3 and Resnet-50 models had similar results, the Resnet-50 had the best result among them. The Resnet-50 classified all test images as 538 true positives (TP), 6 false positives (FP), 543 true negatives (TN), and 11 false negatives (FN). True and false terms are logical results of classification assessment. Positive and negative are also meant images that are with and without people. If images with and without people were classified as true, they were called TP and TN, were classified as false, they were called FP and FN. Some FP and TN image examples of Resnet-50 architecture are respectively shown in Figures 4 and 5.

Furthermore, Table 7 is shown the training times for the three DL architectures. While the training time of DenseNet-169 was the longest, the ResNet-50 was the shortest training time for the REP dataset.

Investigations on false positive images revealed that does not contain a real person and contain human-like materials such as a painting with human figures, plastic mannequins, and sculptures and these images were misclassified by the models. If the misclassified images are removed from the model, there will be no effect on the accuracy of the classification. Because the model will encounter these images in the training process, it will not be able to learn that they are non-human images. If the number of similar images in the dataset is increased, the problem may be solved.

Figure 4. Examples of incorrect (FP) prediction images

Figure 5. Examples of the correct (TN) prediction images

Table 7. Training times of DL models

Model	Training Times(hour)
Resnet-50	~10
DenseNet	~18
Inceptionv3	~11

5. Conclusion

In this study, it is aimed to distinguish images with people among real-estate listing images to preserve human privacy. For this purpose, we applied three state-of-the-art DL architectures namely ResNet, DenseNet, and Inceptionv3 using our novel REP dataset. The results of the study show that the highest accuracy among the three architectures was obtained with the ResNet50 model. The average accuracy of training with all architectures was approximately 98%.

This study can be used at the national and international levels, including the production of all kinds of spatial services and goods for the protection of personal data. For example, it has the potential to produce solutions that can be used effectively by various industries such as tourism, real estate, warehousing, logistics, construction, and the civil and official authorities that supervise them. Moreover, tools such as room classification, price and building age estimation from images can be among the innovative solutions in this sector. In future studies, we aim to separate the images of people and their body parts in photographs to be used in real estate advertisements through digital services and to improve image quality.

Acknowledgement

Trainings and calculations reported in this paper were fully/partially performed at TUBITAK ULAKBIM, High Performance, and Grid Computing Center (TRUBA) resources. This study was supported within the scope of TÜBİTAK 2209-B. Undergraduate Research Projects Support Program for Industry with project number 1139B412100343.

Author contributions

Bülent Bayram: Conceptualization, Methodology, Writing-Reviewing and Editing. **Tolga Bakırman:** Conceptualization, Methodology, Software,Writing-Reviewing and Editing. **Raziye Hale Topaloğlu:** Writing-Reviewing and Editing. **Hilal Adıyaman:** Data curation, Software, Validation, Writing-Original draft preparation. **Yunus Emre Varul:** Data curation, Software, Validation, Writing-Original draft preparation. **Elif Alkan:** Investigation, Data curation, Validation. **Sevgi Zümra Karaca:** Investigation, Data curation, Validation.

Conflicts of interest

The authors declare no conflicts of interest.

References

1. Fields, D., & Rogers, D. (2021). Towards a critical housing studies research agenda on platform real estate. Housing, theory and society, 38(1), 72-94.
2. Kumari, A., Maan, V., & Dhiraj. (2021). A Deep Learning-Based Segregation of Housing Image Data for Real Estate Application. In Intelligent Learning for Computer Vision: Proceedings of Congress on Intelligent Systems 2020 (pp. 165-179). Springer Singapore.
3. Bappy, J. H., Barr, J. R., Srinivasan, N., & Roy-Chowdhury, A. K. (2017, March). Real estate image classification. In 2017 ieee winter conference on applications of computer vision (wacv) (pp. 373-381). IEEE.
4. Azizi, I., & Rudnytskyi, I. (2022). Improving Real Estate Rental Estimations with Visual Data. Big Data and Cognitive Computing, 6(3), 96.
5. Hassanzadeh, Z., Biddle, R., & Marsen, S. (2021). User perception of data breaches. IEEE Transactions on Professional Communication, 64(4), 374-389.
6. Erdos, D. (2022). Identification in personal data: Authenticating the meaning and reach of another broad concept in EU data protection law. Computer Law & Security Review, 46, 105721.
7. Zhang, B., Zou, G., Qin, D., Ni, Q., Mao, H., & Li, M. (2022). RCL-Learning: ResNet and convolutional long short-term memory-based spatiotemporal air pollutant concentration prediction model. Expert Systems with Applications, 207, 118017.
8. Salman, F. M., & Abu-Naser, S. S. (2022). Classification of real and fake human faces using deep learning. International Journal of Academic Engineering Research (IJAER), 6(3), 1-14
9. Krizhevsky, A., Sutskever, I., & Hinton, G. E. (2017). Imagenet classification with deep convolutional neural networks. Communications of the ACM, 60(6), 84-90.
10. Long, J., Shelhamer, E., & Darrell, T. (2015). Fully convolutional networks for semantic segmentation. In Proceedings of the IEEE conference on computer vision and pattern recognition (pp. 3431-3440).
11. Simonyan, K., & Zisserman, A. (2014). Very deep convolutional networks for large-scale image recognition. arXiv preprint arXiv:1409.1556.
12. Szegedy, C., Liu, W., Jia, Y., Sermanet, P., Reed, S., Anguelov, D., ... & Rabinovich, A. (2015). Going deeper with convolutions. In Proceedings of the IEEE conference on computer vision and pattern recognition (pp. 1-9).
13. He, K., Zhang, X., Ren, S., & Sun, J. (2016). Deep residual learning for image recognition. In Proceedings of the IEEE conference on computer vision and pattern recognition (pp. 770-778).
14. Xie, S., Girshick, R., Dollár, P., Tu, Z., & He, K. (2017). Aggregated residual transformations for deep neural networks. In Proceedings of the IEEE conference on computer vision and pattern recognition (pp. 1492-1500).
15. Huang, G., Liu, S., Van der Maaten, L., & Weinberger, K. Q. (2018). Condensenet: An efficient densenet using learned group convolutions. In Proceedings of the IEEE conference on computer vision and pattern recognition (pp. 2752-2761).
16. Zoph, B., Vasudevan, V., Shlens, J., & Le, Q. V. (2018). Learning transferable architectures for scalable image recognition. In Proceedings of the IEEE conference on computer vision and pattern recognition (pp. 8697-8710).
17. Tan, M., & Le, Q. (2019, May). Efficientnet: Rethinking model scaling for convolutional neural networks. In International conference on machine learning (pp. 6105-6114). PMLR.
18. Koch, D., Despotovic, M., Sakeena, M., Döller, M., & Zeppelzauer, M. (2018, June). Visual estimation of building condition with patch-level ConvNets. In Proceedings of the 2018 ACM Workshop on Multimedia for Real Estate Tech (pp. 12-17).
19. Zeppelzauer, M., Despotovic, M., Sakeena, M., Koch, D., & Döller, M. (2018, June). Automatic prediction of building age from photographs. In Proceedings of the 2018 ACM on International Conference on Multimedia Retrieval (pp. 126-134).
20. Zhao, Y., Chetty, G., & Tran, D. (2019, December). Deep learning with XGBoost for real estate appraisal. In 2019 IEEE symposium series on computational intelligence (SSCI) (pp. 1396-1401). IEEE.
21. Kamara, A. F., Chen, E., Liu, Q., & Pan, Z. (2020). A hybrid neural network for predicting Days on Market a measure of liquidity in real estate industry. Knowledge-Based Systems, 208, 106417.
22. Zhou, B., Zhao, H., Puig, X., Xiao, T., Fidler, S., Barriuso, A., & Torralba, A. (2019). Semantic understanding of scenes through the ade20k dataset. International Journal of Computer Vision, 127(3), 302-321.
23. Barhoom, A. M., & Abu-Naser, S. S. (2022). Diagnosis of Pneumonia Using Deep Learning. International Journal of Academic Engineering Research (IJAER), 6(2), 48-68
24. Zhou, L., Pan, S., Wang, J., & Vasilakos, A. V. (2017). Machine learning on big data: Opportunities and challenges. Neurocomputing, 237, 350-361.
25. He, K., Zhang, X., Ren, S., Sun, J. (2016). Identity mappings in deep residual networks. In Lecture Notes in Computer Science (Including Subseries Lecture

Notes in Artificial Intelligence and Lecture Notes in Bioinformatics), 630–645.
26. Bayram, B., Kilic, B., Özoğlu, F., Erdem, F., Bakirman, T., Sivri, S., ... & Delen, A. (2020). A Deep learning integrated mobile application for historic landmark recognition: A case study of Istanbul. Mersin Photogrammetry Journal, 2(2), 38-50.
27. Szegedy, C., Vanhoucke, V., Ioffe, S., Shlens, J., & Wojna, Z. (2016). Rethinking the inception architecture for computer vision. In Proceedings of the IEEE conference on computer vision and pattern recognition (pp. 2818-2826).
28. Degadwala, S., Vyas, D., Biswas, H., Chakraborty, U., & Saha, S. (2021, July). Image captioning using inception V3 transfer learning model. In 2021 6th International Conference on Communication and Electronics Systems (ICCES) (pp. 1103-1108). IEEE.
29. Joshi, K., Tripathi, V., Bose, C., & Bhardwaj, C. (2020). Robust sports image classification using InceptionV3 and neural networks. Procedia Computer Science, 167, 2374-2381.
30. Sam, S. M., Kamardin, K., Sjarif, N. N. A., & Mohamed, N. (2019). Offline signature verification using deep learning convolutional neural network (CNN) architectures GoogLeNet inception-v1 and inception-v3. Procedia Computer Science, 161, 475-483.
31. Gunawan, A. A., & Surya, K. (2018). Brainwave classification of visual stimuli based on low-cost EEG spectrogram using DenseNet. Procedia Computer Science, 135, 128-139.
32. Chollet, F. (2015). Keras: Deep learning for humans, Github. https://github.com/keras-team/keras

Mersin Photogrammetry Journal
https://dergipark.org.tr/en/pub/mephoj
e-ISSN 2687-654X

Adaptation analysis of produced 3D models from UAV-SLAM and UAV-TLS data combinations

Kasım Erdal [1], **Hasan Bilgehan Makineci** [*1]

[1]*Konya Technical University, Department of Geomatics Engineering, Türkiye*

Keywords
SLAM
TLS
UAV
ICP

Research Article
DOI:10.53093/mephoj.1269630

Received:23.03.2023
Revised: 09.04.2023
Accepted:11.04.2023
Published:27.05.2023

Abstract

Photogrammetric techniques are widely used to represent the characteristics of historical buildings in the digital environment in the closest way to reality. Terrestrial photogrammetric methods have needed different alternatives in recent years to produce 3D models that offer high reality. In recent years, producing point data with the Terrestrial Laser Scanner (TLS), Unmanned Aerial Vehicles (UAV) images, and alternative methods such as the Simultaneous Localization and Mapping (SLAM) algorithm has become popular. Aligning point data from different approaches and making 3D models create new problems. Primarily, it is necessary to investigate the operations performed manually by the operator over time. Also, it is needed to explore the integration of automatic algorithms such as Iterative Closest Point (ICP) in terms of accuracy. In this research, point data of the Dokuz Historical Bridge was produced using different aligning techniques manually and automatically with the ICP algorithm. The assessment has been done from the results of combined point data over time and accuracy. In both UAV-TLS and UAV-SLAM aligning procedures, spatial accuracy was determined as 2.8cm and 4cm, respectively, in the operations performed by the operator and 46cm and 12cm in the procedures performed automatically by ICP. As a result, it was determined that the operators combined produced better findings, especially in research including coordinate transform.

1. Introduction

Cultural heritages contain the experiences and traditions of the society in the past years and play a leading role in transferring this structure to future generations [1]. For this reason, cultural heritages constitute the identity structure of the society [2]. An important part of cultural heritage is historical artifacts. Madrasahs, mosques, churches, statues, bridges, etc. are shown as examples of historical works [3].

Among the photogrammetric methods, the most preferred terrestrial photogrammetry technique in the documentation of architectural works, regardless of the size of the object, generating 3D models and point data using images obtained from different camera angles from the earth [4], has been used as a complementary method in other research subjects in recent years with the developing technology [1,2,4]. Terrestrial Laser Scanners (TLS) are used more frequently in 3D modeling of historical buildings and in obtaining point clouds [5]. In addition to TLS, the Simultaneous Localization and Mapping-SLAM algorithm, another technique to be fast, practical, and will allow robotic mapping in the future, can also be used in the interiors of historical buildings, etc. It is known to be used for studies [6]. It is also known in the literature that in almost all photogrammetric methods, it is difficult to obtain data on the upper parts of the structures, such as the roof, and to determine the details of the structure [7,8]. Using the mentioned techniques, studies are carried out with Unmanned Aerial Vehicles (UAV) integrated systems, and the results obtained in these studies provide final products with high location-based accuracy [9].

Today, UAVs are used in many fields, such as agriculture, industry, archaeological and architectural studies, and entertainment purposes. UAVs are preferred in the mapping industry and especially in photogrammetric studies, thanks to their autonomous and semi-autonomous use, the payloads they can carry, and the GNSS-IMU system [10].

Iterative Closest Point (ICP) is an algorithm for measuring similarities between two-point clouds and aligning these point clouds with each other. Usually, the first point cloud is created by scanning a real object,

* **Corresponding Author**
(kerdal.245@gmail.com) ORCID ID 0000-0001-6024-7361
*(hbmakineci@ktun.edu.tr) ORCID ID 0000-0003-3627-5826

Cite this article
Erdal, K., & Makineci, H. B. (2023). Adaptation analysis of produced 3D models from UAV-SLAM and UAV-TLS data combinations. Mersin Photogrammetry Journal, 5(1), 18-23

while the second point cloud is a virtual point cloud produced by a model [11]. ICP is a widely used algorithm, particularly in robotics, 3D modeling, and object recognition [12,13].

In this research, point data from the historical bridge consisting of a single bridge arch and an additional stone bridge wall with an estimated construction date of 1998 belonging to the State Hydraulic Works (DSI) was produced using TLS and a mobile device application based on the SLAM algorithm. The upper part of the bridge was produced from UAV data with a photogrammetric flight plan. Point data were obtained from UAV images, and point data was produced by TLS and SLAM algorithms separately. The operator combines manual joining and the Iterative Closest Point (ICP) algorithm. The results were compared to perform a spatial accuracy analysis.

2. Method

The technical equipment used in the research, the study area, and the algorithms used are presented in this section. The continuation of this section includes the findings and discussions.

2.1. Terrestrial laser scanner

Faro Focus 3D X330 equipment was used in the study (Figure 1). The TLS provides a 3D image by scanning indoor and outdoor scans quickly and in detail.

Figure 1. FaroFocus 3D X 330

The scanning process is carried out by deflecting the infrared laser beam sent to the center of the TLS rotating mirror to the scanned environment, the receiver of the TLS receives the beam reflected from the surrounding objects, and the scanning process is completed. TLSs differ in themselves as a distance measurement method. The TLS distance measurement methods used in the study work with the phase comparison method. The phase comparison method determines the distance between TLS and the object by measuring the phase differences. TLS amplitude modulation working with the phase comparison method emits one wave, and this modulation includes several wavelengths [5,14]. The distance between TLS and the object is determined by calculating the phase difference between the transmitted and received signals (Figure 2).

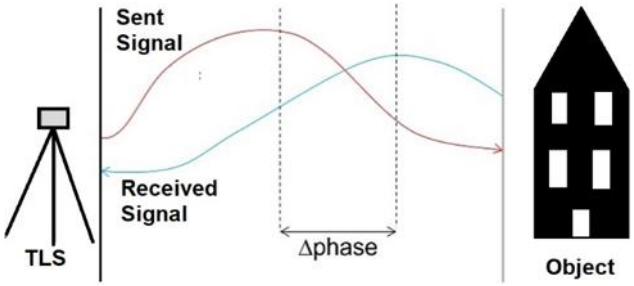

Figure 2. Phase difference distance measuring method

2.2. SLAM based the mobile application

The SLAM is an algorithm that simultaneously analyzes the current location of the autonomous vehicle or mobile system while creating a map of the environment in autonomous vehicles or mobile systems [15]. While mapping and positioning were solved separately in recent years, today, they are solved simultaneously with the SLAM algorithm [16]. Lidar, sonar, IMU, IR, camera, and GNSS support the SLAM algorithm. Systems using the SLAM algorithm work fast, safely, and with fewer errors [17]. The SLAM algorithm is used in autonomous driving electric vehicles, backpack lidar systems, unmanned aerial vehicles, smart home appliances, and smartphones. In this study, it is done by visual slam application with Iphone brand smartphone. Application works in this algorithm:

1. Turn around the object with camera in a specific distance and use GCPs in camera frame,
2. Then specify the object with one tour of around the object and,
3. Create point cloud from that data, taken from object.

In order to use a mobile application based on the SLAM algorithm, the iPhone 11 smartphone was preferred in this research. The smartphone has a camera and GNSS supporting the SLAM algorithm, and the SLAM algorithm was used successfully while obtaining images photogrammetrically (Figure 3) [18].

2.3. Unmanned aerial vehicle

The study used the Rotary wing Parrot Anafi as the UAV (Figure 4). With a total take-off weight of 320 g, Anafi is suitable for 3D modeling works for photogrammetric purposes, thanks to its small size, ease of use, and speed. In addition, since it is classified as a toy by the General Directorate of Civil Aviation (GDCA), it is preferred because it can be flown without legal permission.

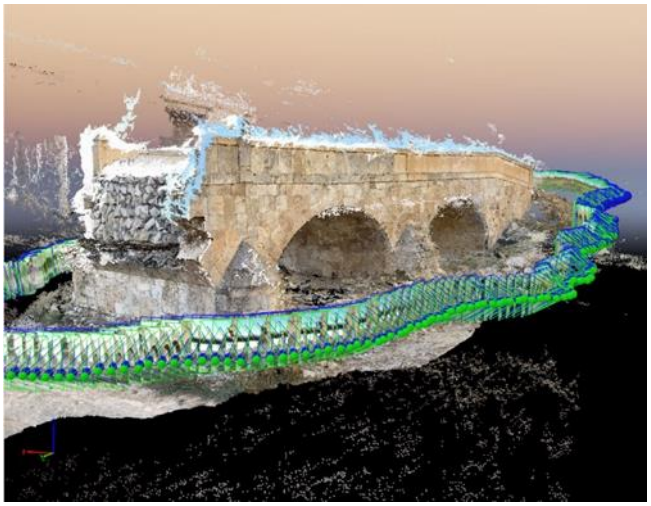

Figure 3. SLAM application

Table 1. Parrot ANAFI Specs

Weight	320 gr
Max. Communication Distance	4 km
Max. Flight Time	25 min.
Wind Resistance	14 m/sec
Max. Vertical Speed	4 m/sec
Max. Horizontal Speed	15 m/sec
Integrated RGB Camera	1'' CMOS 20 MP

Figure 4. Parrot Anafi

The images obtained after the UAV flight performed with photogrammetric-based flight planning are evaluated by software containing newly developed image processing techniques. Such software has complex algorithms using the Structure from Motion (SfM) algorithm [6].

According to photogrammetric acquisition techniques, the SFM algorithm allows obtaining the 3D structure of an object whose side and forward overlapped images were taken in the digital environment [19,20]. Digital surface model, orthophoto and 3D model of cultural heritages can be created with photogrammetric acquisition techniques [21,23].

2.4. The data obtained from object

A total of ten Ground Control Points (GCP) has been positioned, eight are around the historic bridge, and two are on the bridge's road surface. GCPs measured with Continuously Operating Reference Station (CORS) technic. The GCPs were measured at TM 3° projection, 33° slice of ITRF 96 datum (Figure 5).

Figure 5. GCP Measurement

In order to obtain point data on the upper surface of the historic bridge, a UAV flight was carried out. The flight carried out in an area of 400 m^2, took 3 minutes and 37 seconds. The ground sampling distance (GSD) in the flight performed at an altitude of 10 m is 0.39 cm/px (Figure 5). Point data consisting of 12.044.504 points was obtained by balancing the 105 images obtained after the flight in the software. The software performs the adjustment process using the SFM algorithm.

With TLS, the historical bridge, including the side wall above the arc, the arc's outer surface, and the arc's inner surface (in short, all parts except the road part), were scanned. The session plan of the related scan is presented in Figure 7.

The TLS was positioned at six points in the planned session, and scanning was performed. Sessions lasted between 8 and 9 minutes on average. The collected data were adjusted in a software (SCENE), and merged point cloud data was obtained.

The point cloud of all parts of the historical bridge was obtained from the field without coordinates. The obtained data were balanced and transferred to Cloud Compare software in order to convert them to a geodetic coordinate system and combine point clusters.

2.5. ICP algorithm

The ICP algorithm initially applies transformation operations to minimize the differences between the point

clouds. This process involves iteratively updating the transformation matrix, which aligns point clouds to each other. The ICP algorithm minimizes the least squares error function between the first- and second-point clouds. This increases the accuracy of the alignment process and improves the final alignment result.

Figure 6. The photogrammetric flight plan of UAV and study area

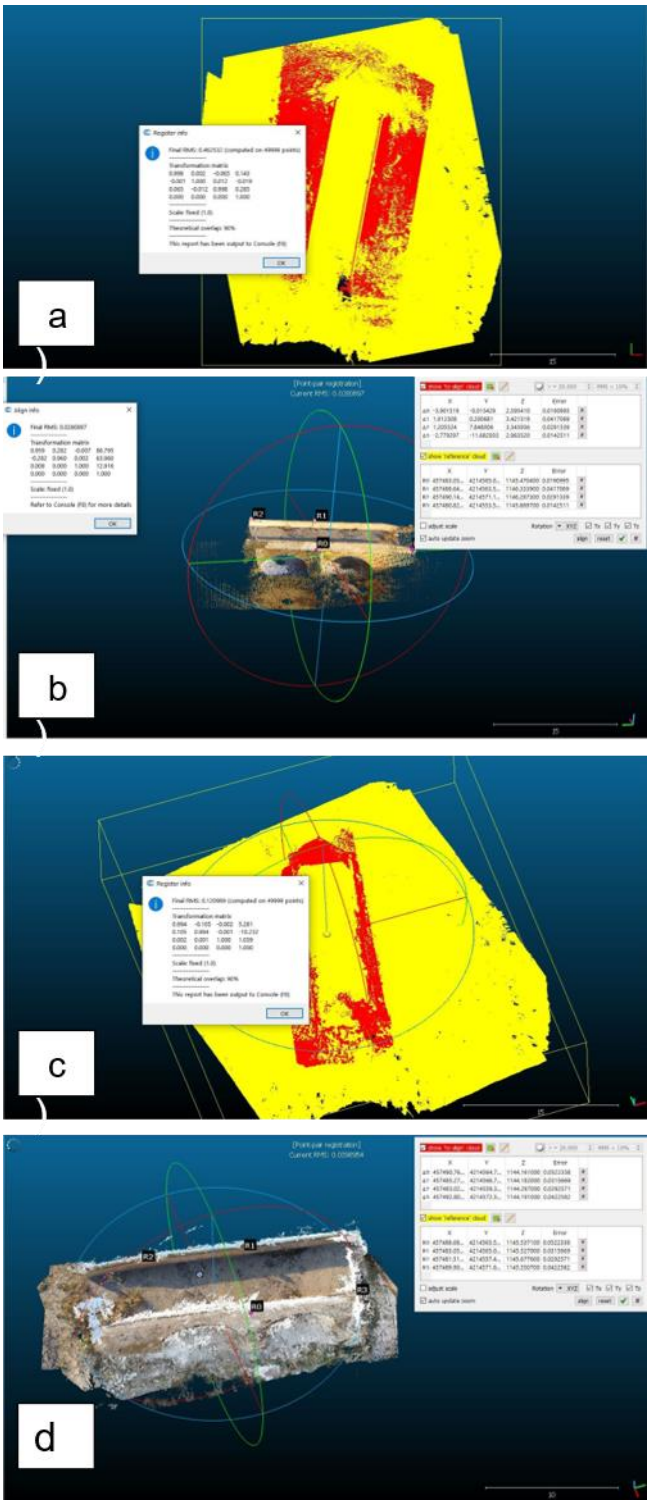

Figure 8. Alignment results (RMSE) of the study (a: UAV-TLS with ICP, b: UAV-TLS manually by operator, c: UAV-SLAM with ICP, d: UAV-SLAM manually by operatör)

3. Results

Point data from UAV images, point cloud obtained by aligning TLS sessions, and point data produced with the SLAM algorithm were combined in Cloud Compare software with two different methods. The first method made by the operator according to their visual suitability is called manual combination, and the combination performed automatically by the ICP algorithm is called the ICP combination. Cloud Compare, the free and open-source software used for aligning point data, offers a relative accuracy for the obtained point clouds. This accuracy is revealed by calculating the root mean square error (RMSE) between the points within the system itself

(Figure 8). The alignment results of two different methods are presented in Table 2.

Table 2. General comparative findings (RMSE)

Data Type	Accuracy (m)	
	Manually	ICP
UAV-TLS	0.028	0.462
UAV-SLAM	0.040	0.121

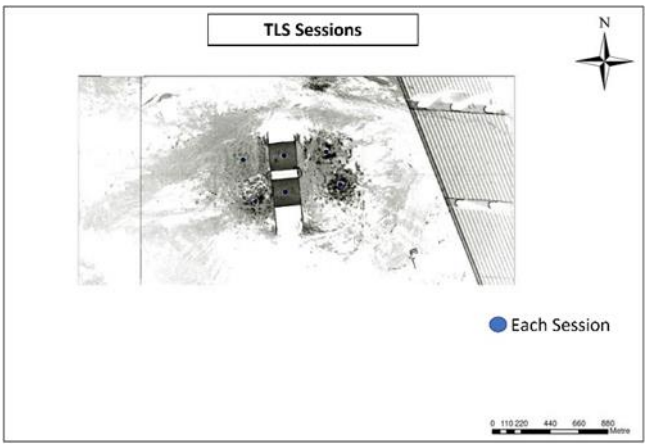

Figure 7. The TLS session plan

Although the visual combination results are satisfactory, the findings obtained regarding positional accuracy show that the manual method provides high accuracy.

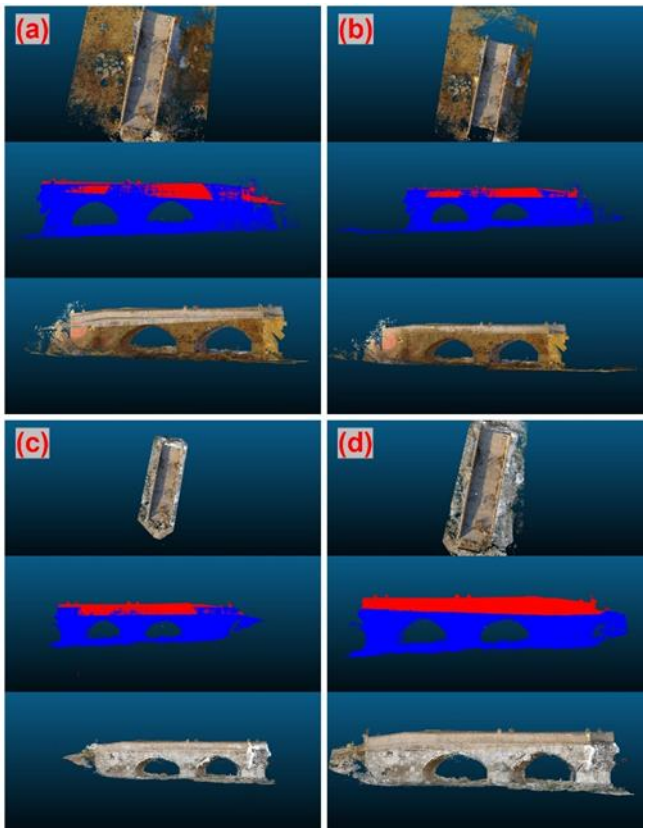

Figure 9. Alignment of point data (a: UAV-TLS with ICP, b: UAV-TLS manually by operator, c: UAV-SLAM with ICP, d: UAV-SLAM manually by operator)

Point data obtained from the ICP algorithm combined with UAV and TLS data is presented in Figure 9a. The combination time of the algorithm is 11 minutes and 27 seconds; the model accuracy is 46 cm. When the operator combined the same data manually, the process took 22 minutes and 43 seconds, and the model accuracy was 3 cm (Figure 9b).

Additionally, point data obtained from the ICP algorithm combined with UAV and SLAM data is presented in Figure 9c. The combination time of the algorithm is 08 minutes and 33 seconds; the model accuracy is 13 cm. When the operator combined the same data manually, the process took 19 minutes and 57 seconds, and the model accuracy was 4 cm (Figure 9d).

4. Discussion

It has been seen that the ICP algorithm, which can combine automatic point clouds, provides users with significant time savings while giving critical negative results in model accuracy. Both types of aligning offer visually positive results. However, the combined time-model coordinate linear relationship reveals the inverse relationship between operator coupling and ICP algorithm aligning.

In the absence of similar working principles of point-generating sources, the accuracy of automatic aligning decreases relatively. For this reason, in aligning point clouds obtained from different data sources, manual alignment by the operator takes longer than the ICP but with higher accuracy.

5. Conclusion

In the research, the 3D model of the historic bridge in the Dokuz District of Konya was produced using a mobile device application based on the UAV, TLS, and the SLAM algorithm. The operator combined point data manually and automatically using the ICP algorithm. Both methods determined that manual aligning by the operator gave more accurate results than the automatic aligning technic with the ICP algorithm.

Author contributions

Hasan Bilgehan Makineci: Conceptualization, Methodology, Data curation, Writing-Original draft preparation, Software, Validation. **Kasım Erdal:** Visualization, Investigation, Writing-Reviewing and Editing.

Conflicts of interest

The authors declare no conflicts of interest.

References

1. Şenol, H. İ., Yiğit, A. Y., Kaya, Y., & Ulvi A. (2021). İHA ve yersel fotogrametrik veri füzyonu ile kültürel mirasın 3 boyutlu (3B) modelleme uygulaması: Kanlıdivane Örneği. Türkiye Fotogrametri Dergisi, 3(1), 29-36.

2. Şanlıoğlu, İ., Zeybek, M., & Karauğuz, G. (2013). Photogrammetric survey and 3D modeling of Ivriz rock relief in Late Hittite Era. Mediterranean Archaeology & Archaeometry, 13(2), 147-157.
3. Yiğit, A. Y., & Ulvi, A. (2020). İHA fotogrametrisi tekniği kullanarak 3B model oluşturma: Yakutiye Medresesi Örneği. Türkiye Fotogrametri Dergisi, 2(2), 46-54.
4. Karasaka, L., Makineci, H. B., & Erdal, K. (2023). Accuracy assessment toward mergıng of terrestrıal laser scanner poınt data and unmanned aerıal system poınt data. Konya Journal of Engineering Sciences, 11(1), 124-135.
5. Karasaka, L., & Beg, A. A. R. (2021). Yersel lazer tarama yöntemi ile farklı geometrik yapıdaki özelliklerin modellenmesi. Geomatik, 6(1), 54-60.
6. Sun, P., Zhou, F., Sun, J., & Wang, L. (2021). High-accuracy three-dimensional measurement based on multi-directional cooperative target with weighted SfM algorithm. Measurement, 172, 108955.
7. Ulvi, A., Yakar, M., Yiğit, A., & Kaya, Y. (2019). The use of photogrammetric techniques in documenting cultural heritage: The Example of Aksaray Selime Sultan Tomb. Universal Journal of Engineering Science, 7(3), 64-73.
8. Ulvi, A., Yakar, M., Yiğit, A. Y., & Kaya, Y. (2020). İHA ve yersel fotogrametrik teknikler kullanarak Aksaray Kızıl Kilise'nin 3 Boyutlu nokta bulutu ve modelinin üretilmesi. Geomatik, 5(1), 22-30.
9. Yakar, M., Ulvi, A., Yiğit, A. Y., & Alptekin, A. (2022). Discontinuity set extraction from 3D point clouds obtained by UAV Photogrammetry in a rockfall site. Survey Review, 1-13.
10. Makineci, H. B. (2016). İnsansız hava araçları lidar etkileşimi. Geomatik, 1(1), 19-23.
11. Yao, Z., Zhao, Q., Li, X., & Bi, Q. (2021). Point cloud registration algorithm based on curvature feature similarity. Measurement, 177, 109274.
12. Wakisaka, E., Moribe, Y., & Kanai, S. (2019). TLS point cloud registration based on ICP algorithm using point quality. The International Archives of the Photogrammetry, Remote Sensing and Spatial Information Sciences, 42, 963-968.
13. Si, H., Qiu, J., & Li, Y. (2022). A review of point cloud registration algorithms for laser scanners: applications in large-scale aircraft measurement. Applied Sciences, 12(20), 10247.
14. Yılmaz, H. M., & Yakar, M. (2006). Yersel lazer tarama Teknolojisi. Yapı teknolojileri Elektronik dergisi, 2(2), 43-48.
15. Demir, M. N., & Altun, Y. (2020). Otonom Araçla Genetik Algoritma Kullanılarak Haritalama ve Lokasyon. Düzce Üniversitesi Bilim ve Teknoloji Dergisi, 8(1), 654-666.
16. Begum, M., Mann, G. K., & Gosine, R. G. (2008). Integrated fuzzy logic and genetic algorithmic approach for simultaneous localization and mapping of mobile robots. Applied Soft Computing, 8(1), 150-165.
17. Sualeh, M., & Kim, G. W. (2019). Simultaneous localization and mapping in the epoch of semantics: a survey. International Journal of Control, Automation and Systems, 17(3), 729-742.
18. Tavani, S., Billi, A., Corradetti, A., Mercuri, M., Bosman, A., Cuffaro, M., ... & Carminati, E. (2022). Smartphone assisted fieldwork: Towards the digital transition of geoscience fieldwork using LiDAR-equipped iPhones. Earth-Science Reviews, 227, 103969.
19. Ahmadabadian, A. H., Yazdan, R., Karami, A., Moradi, M., & Ghorbani, F. (2017). Clustering and selecting vantage images in a low-cost system for 3D reconstruction of texture-less objects. Measurement, 99, 185-191.
20. Yakar, M., & Dogan, Y. (2019). 3D Reconstruction of Residential Areas with SfM Photogrammetry. In Advances in Remote Sensing and Geo Informatics Applications: Proceedings of the 1st Springer Conference of the Arabian Journal of Geosciences (CAJG-1), Tunisia 2018 (pp. 73-75). Springer International Publishing.
21. Alptekin, A., & Yakar, M. (2021). 3D model of Üçayak Ruins obtained from point clouds. Mersin Photogrammetry Journal, 3(2), 37-40.
22. Mohammed, O., & Yakar, M. (2016). Yersel Fotogrametrik Yöntem İle İbadethanelerin Modellenmesi. Selcuk University Journal of Engineering Sciences, 15(2), 85-95.
23. Kanun, E., Alptekin, A., Karataş, L., & Yakar, M. (2022). The use of UAV photogrammetry in modeling ancient structures: A case study of "Kanytellis". Advanced UAV, 2(2), 41-50.
24. Alyilmaz, C., Alyilmaz, S., & Yakar, M. (2010). Measurement of petroglyhps (rock of arts) of Qobustan with close range photogrammetry. International Archives of Photogrammetry, Remote Sensing and Spatial Information Sciences, 38(Part 5), 29-32.
25. Korumaz, A. G., Dülgerler, O. N., & Yakar, M. (2011). Kültürel mirasin belgelenmesinde dijital yaklaşimlar. Selçuk Üniversitesi Mühendislik, Bilim ve Teknoloji Dergisi, 26(3), 67-83.

Mersin Photogrammetry Journal
https://dergipark.org.tr/en/pub/mephoj
e-ISSN 2687-654X

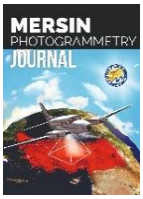

Connected pixels-based image smoothing filter

Erkan Besdok *[1], **Pinar Civicioglu**[2]

[1]Erciyes University, Department of Geomatics Engineering, Türkiye
[2]Erciyes University, Department of Aircraft Electrics and Electronics, Türkiye

Keywords
Connected Pixels
Image Smoothing
Bezier Search Optimization Algorithm

Research Article
DOI: 10.53093/mephoj.1279877

Received:09.04.2023
Revised: 05.05.2023
Accepted:08.05.2023
Published:27.05.2023

Abstract

Digital image processing heavily relies on the connectivity of pixels, as it is a vital component for accurate object identification and analysis within an image. Grouping together pixels with similar features such as colour and intensity, allows for the formation of meaningful patterns or objects, which is essential for object recognition and segmentation. This approach is particularly valuable in photogrammetric imaging, video surveillance, deep learning as it facilitates the isolation of regions of interest and object tracking. Image smoothing is also a crucial aspect in enhancing visual quality by reducing noise and enhancing details, especially in applications such as aerial mapping, medical imaging, video compression, image resizing and computer vision. The absence of connected pixels and image smoothing would make image processing tasks more challenging and less reliable, making them fundamental to digital image processing and critical to various applications in diverse fields. This paper introduces a novel image smoothing filter called Connected Pixels Based Image Smoothing Filter (CPF), which is based on gray connected pixels. The success of the CPF was compared to that of the Non-Local Means Filter (NLMF) in terms of Structural Similarity Index (SSIM) for the same Mean Squared Error (MSE). The experimental results showed that CPF has a better ability to preserve image details compared to NLMF.

1. Introduction

Pixel connectivity refers to the relationship between neighboring pixels in a digital image. It is a fundamental concept in image processing and computer vision, as it plays a crucial role in many image analysis tasks such as edge detection, segmentation, and object recognition [1-5]. In general, pixel connectivity refers to the notion of how pixels are connected or related to each other. There are different ways to define pixel connectivity, depending on the context and the specific requirements of the image processing task at hand [6-9]. One of the most common definitions of pixel connectivity is based on the notion of adjacency, which refers to whether two pixels are neighbors or not. In a 2D image, two pixels are considered adjacent if they are located next to each other horizontally, vertically, or diagonally [10-12]. In other words, two pixels are adjacent if they share a common edge or corner. Pixel connectivity is often quantified using a connectivity matrix or a connectivity graph, which represents the relationships between adjacent pixels in the image. A connectivity matrix is a binary matrix that encodes the adjacency relationships between pixels, where a value of 1 indicates that two pixels are adjacent, and a value of 0 indicates that they are not. A connectivity graph, on the other hand, is a graph-theoretic representation of the connectivity matrix, where each pixel is represented as a vertex, and the adjacency relationships between pixels are represented as edges. The definition of pixel connectivity can also be extended to 3D images, where it refers to the relationships between neighboring voxels (3D pixels). In a 3D image, two voxels are considered adjacent if they are located next to each other in any of the three spatial dimensions (x, y, z). Pixel connectivity is closely related to other concepts in image processing, such as image topology and morphological operations. In image topology, the connectivity of a set of pixels is defined as the number of connected components in the set. Morphological operations, such as dilation and erosion,

* **Corresponding Author**
*(ebesdok@erciyes.edu.tr) ORCID ID 0000-0001-9309-375X
(civici@erciyes.edu.tr) ORCID ID 0000-0003-1850-8489

Cite this article
Beşdok, E., & Civicioğlu, P. (2023). Connected pixels-based image smoothing filter. Mersin Photogrammetry Journal, 5(1), 24-31

rely on the notion of pixel connectivity to manipulate the shapes and boundaries of objects in an image. In conclusion, pixel connectivity is a fundamental concept in image processing and computer vision that refers to the relationships between neighboring pixels in a digital image. It plays a crucial role in many image analysis tasks, and it is quantified using connectivity matrices or graphs [13-16]. The definition of pixel connectivity can be extended to 3D images, and it is closely related to other concepts in image processing such as image topology and morphological operations. Algorithms developed to find connected pixels can be slow for several reasons. Large image sizes require significant processing time, as the algorithm must check each pixel and its neighbors for connectivity. Complex algorithms also take longer to execute, while outdated hardware may not handle the algorithm efficiently. The data structure used to store the image and pixels can impact the algorithm's speed if not optimized, and inefficient implementation can slow processing time. Optimization of these factors may result in faster processing times for algorithms designed to find connected pixels [17-22].

The process of identifying and labeling subsets of connected components based on a given heuristic is referred to as connected-component labeling, also known as connected-component analysis, region labeling, blob extraction, region extraction, or blob discovery. This algorithmic application is based on graph theory and aims to assign unique labels to each subset of connected components. It is important to note that connected-component labeling should not be mistaken for segmentation.

There are several algorithms [19, 23-31] that can be used to find connected gray pixels in an image. Here are a few:

1. Flood fill algorithm: This is a simple algorithm that starts from a given seed pixel and fills all adjacent pixels of the same gray value. It continues until all connected pixels are filled.
2. Depth-first search (DFS): This is a graph traversal algorithm that can be used to find all connected gray pixels in an image. It starts at a given seed pixel and explores as far as possible along each branch before backtracking.
3. Breadth-first search (BFS): This is another graph traversal algorithm that can be used to find connected gray pixels. It explores all the neighboring pixels at the current level before moving on to the next level.
4. Connected component labelling (CCL): This is a more complex algorithm that assigns a unique label to each connected component of gray pixels in an image. It can be used to identify and separate multiple connected regions with different gray values [28, 32-35].

In this paper, we introduce the Connected Pixels Based Image Smoothing Filter (CPF), which was developed using gray connected pixels. CPF can produce a smoothed image while preserving the detail information in the original image relatively well. It is a simple and effective image smoothing filter that can be easily adapted to different applications due to its simple structure.

The rest of this paper is organized as follows: In Section 2, Connected Pixels Based Image Smoothing Filter (CPF) is mentioned. In Section 3, Experiments are presented. In Section 4, Results and Conclusions are given.

2. Connected pixels-based image smoothing filter (CPF)

This section introduces the Connected Pixels Based Image Smoothing Filter (CPF). CPF is a non-recursive, non-iterative, non-linear image-smoothing filter. CPF uses the median value of the gray-connected pixels to the central pixel of the sliding window to generate the smoothed value of the central pixel. CPF has two parameters: '*win*' and '*T*', which denote the size of the sliding window and the threshold value, respectively. The result obtained is not affected by the order in which neighbors are selected, as long as they meet the threshold requirement. The algorithmic structure of the CPF is shown in Figure 1.

Input: img, win, T
Output: q

$w0 = (win - 1)/2$
$img := padarray(img)$
$[M, N, Dim] \leftarrow size(img)$
for *i=1:Dim* **do**
  $BandImg = img(:, :, i)$
  for *j=w0+1:M-w0* **do**
    for *k=w0+1:N-w0* **do**
      $Temp = BandImg(j - w0 : j + w0, k - w0 : k + w0)$
      $centerpixel = Temp(w0 + 1, w0 + 1)$
      $BinaryImg = |Temp - centerpixel)| \leq T$
      Generate the pixel labels for $BinaryImg$ by using Eq.s 1-2
      Get the pixels, u, that have same label with center pixel of $Temp$
      $q(j, k, i) := median(u)$
    end
  end
end
$q = q(w0 + 1 : end - w0, w0 + 1 : end - w0, :)$

Figure 1. Pseudo-Code of the Connected Pixels Based Image Smoothing Filter (CPF)

Connected component labeling is a crucial process in computer vision, particularly for object recognition. It entails identifying regions in a binary image where pixels are connected. To perform this operation on a 2D image stored in a 2D array, we scan each pixel one by one and assign a label based on the labels of its neighbors or a new label if all its neighbors are background pixels. Suppose a pixel with a value of 0 in array I represents a background pixel, while a pixel with a value of 1 represents an object pixel. To store the labels, we use an array L of the same size as I. In our implementation, we use a single array to hold both I and L. The goal is to fill the array L with integer labels so that object pixels neighboring each other have the same label. Although we use integer labels for simplicity, other label types can also be used. In this paper, we utilized the mask topology presented in Figure 2 of Rosenfeld for an 8-pixel neighborhood based connected pixel labelling [36]. The pixel in the scan mask is represented by letters a, b, c, d, and e, and we use the same letters instead of their (i, j) coordinates.

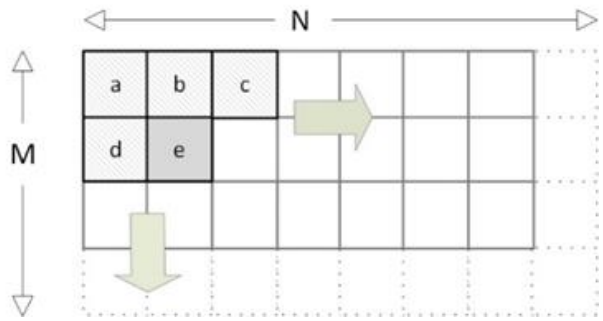

Figure 2. The mask topology of Rosenfeld for 8 pixels neighborhood.

Figure 3 provides an illustrative example of 8-connected component labeling using the Rosenfeld algorithm.

L[e] represents the label of the current pixel being scanned, and I[b] represents the pixel value of the neighbor directly above e in the vertical direction. We start with an integer variable l initialized to 1. During the first scan, we provisionally assign a label to e as follows: L[e] is assigned 0 if I[e] = 0. If a, b, c, and d in the scan mask are all background pixels, we assign it a new label l, and we increment l by 1. Otherwise, we assign it the minimum of the provisional labels already assigned to the scan mask. This process ensures that all pixels in the same object are assigned the same provisional label. In subsequent scans, we change the labels of object pixels to the minimum labels of their neighboring object pixels. Specifically, if L[e] is greater than the minimum of L[b], L[c], and L[d], we update L[e] to the minimum value. We repeat this process until there are no more changes to the labels. In conclusion, connected component labeling is a fundamental operation in computer vision that involves identifying regions in a binary image where pixels are connected. By scanning each pixel and assigning labels based on the labels of its neighbors, we can accurately identify these regions. This technique can be applied to a wide range of applications, including object recognition and image segmentation.

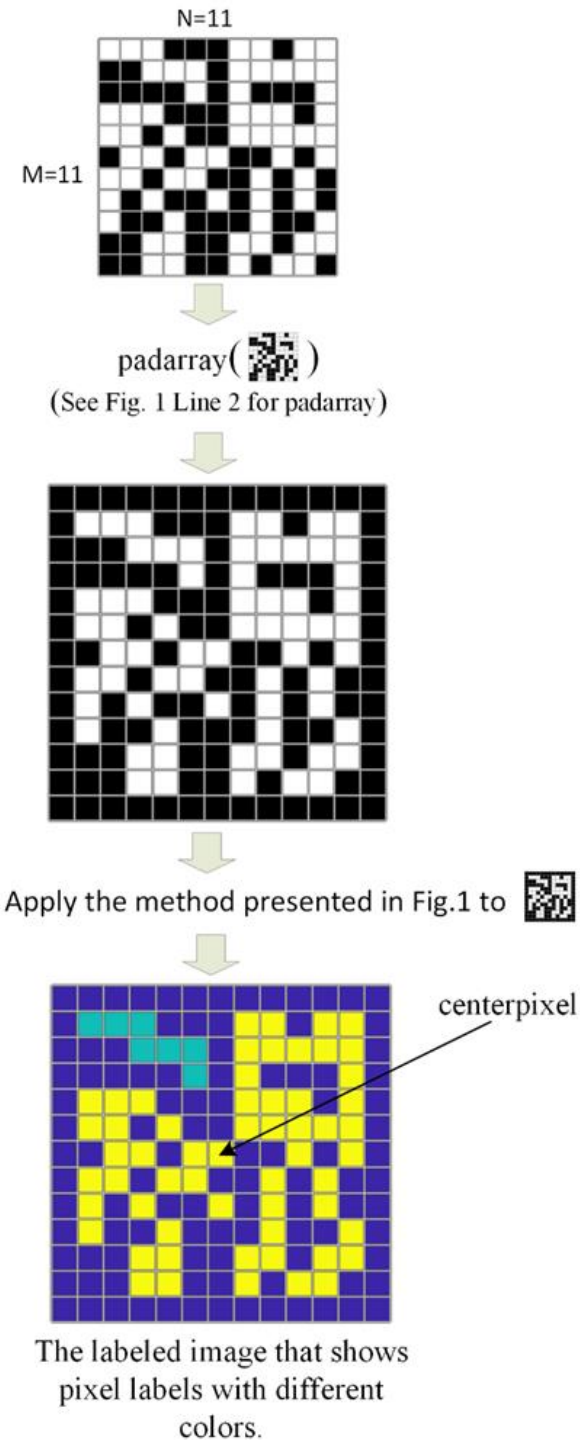

Figure 3. An example of 8-connected component labeling using the Rosenfeld algorithm

Expressing the assignment of a provisional label for "e" during the initial scan can be described by using Equations 1-2.

$$L[e] \leftarrow \begin{cases} 0 & I[e] = 0 \\ l, (l \leftarrow l + 1) & \forall i \in (a,b,c,d),\ I[i] = 0 \\ \underbrace{min}_{i \in (a,b,c,d) \mid I(i)=1} \left(L(i)\right) & otherwise \end{cases} \quad (1)$$

Where

$$L[e] \leftarrow \underbrace{min}_{i \in (a,b,c,d) \mid I[i]=1} \left(L(i)\right), \quad If\ I[e] = 1, \quad and\ \exists i \in (a,b,c,d)\ such\ that\ I[i] = 1 \quad (2)$$

3. Experiments

In this section, we test the success of the Connected Pixels Image Smoother Filter (CPF) in smoothing images using Test Images. The Test Images used are 8-bit RGB with dimensions of 512x512 pixels. We compare the image smoothing capability of CPF to that of the Non-Local Mean Filter [37, 38] for an unbiased review. The smoothing parameter of NLMF is optimized using BSD [39] so that the MSE values calculated between the original image and the smoothed images calculated by CPF and NLMF are the same. Bernstein-Search Differential Evolution (BSD) is a nature-inspired optimization algorithm that is widely used for solving complex problems in various fields such as engineering, finance, and artificial intelligence. BSD combines the concepts of Bernstein polynomials and Differential Evolution to improve the search process for finding the optimal solution. BSD uses a population-based approach where each individual represents a candidate solution, and the optimization process involves generating new candidate solutions through mutation and crossover operations. BSD has shown significant improvements in convergence speed and solution quality compared to traditional optimization algorithms. Overall, BSD is a powerful optimization technique that can be used to solve a wide range of problems efficiently.

The Anisotropic Diffusion filter [40] is an image processing technique used to enhance images by reducing noise while preserving edges. It works by diffusing the image while applying less diffusion to edges and more diffusion to flat regions. This helps to remove noise without blurring edges, resulting in a sharper and clearer image. The degree of diffusion is controlled by a parameter called the diffusion coefficient, which can be adjusted to achieve the desired level of smoothing. Anisotropic diffusion is commonly used in computer vision, medical imaging, and other applications where image clarity is important. The image smoothing performance of CPF and Anistropic Diffusion is tested using the Susskind Test Image and the results are shown in Figure 4.

CPF produced better results than Anistropic Diffusion even in edge regions.

The Non-Local Mean Filter (NLMF) is a popular image denoising technique used to reduce noise while preserving edges and details. Unlike traditional filters that operate on a pixel-by-pixel basis, NLMF considers the entire image when calculating the similarity between patches of pixels. By comparing similar patches, the filter can identify and remove noise while preserving image structure. The algorithm is computationally expensive, but several optimizations have been proposed to improve efficiency. NLMF has been successfully applied to a variety of image processing tasks, including video denoising, image deblurring, and super-resolution. NLMF has three parameters: 'win1', 'win2', and 'S'. 'win1' and 'win2' denote the match and search window sizes, respectively, while 'S' represents the smoothing parameter. Within this section, the notation NLMF (win1, win2, S) will be employed to denote the Non-Local Means Filter along with its corresponding parameters. Similarly, the notation CPF (win, T) will be utilized to represent the Constrained Parametric Filters along with its associated parameters. In the experiments carried out, Mean Squared Error (MSE) and Structural Similarity Index (SSIM) were used to measure the similarities of NLMF and CPF with the original image.

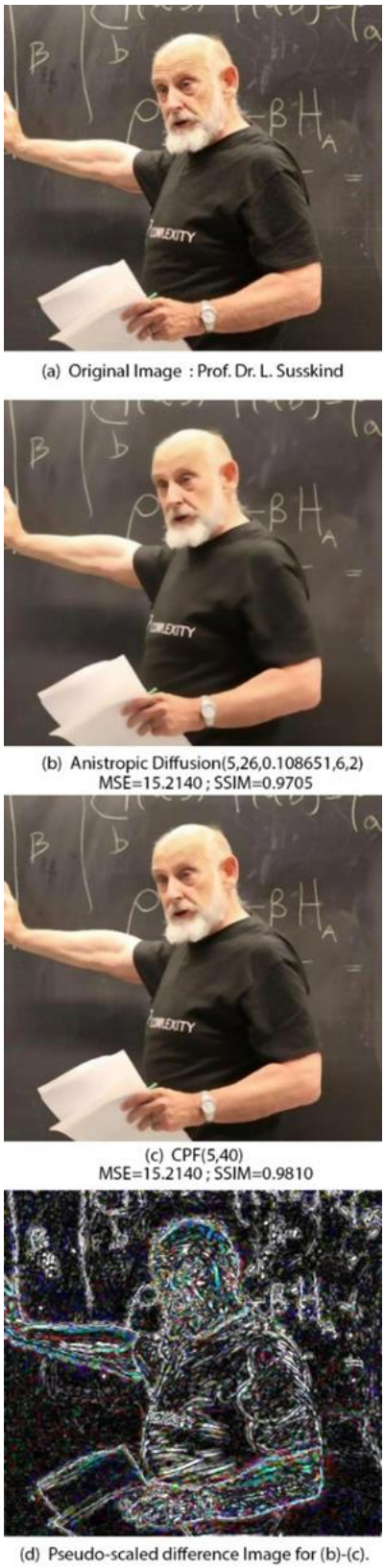

Figure 4. Comparison of CPF and Anistropic Diffusion for the same MSE values on Susskind Test Image (Please use zoom in to see details in the image)

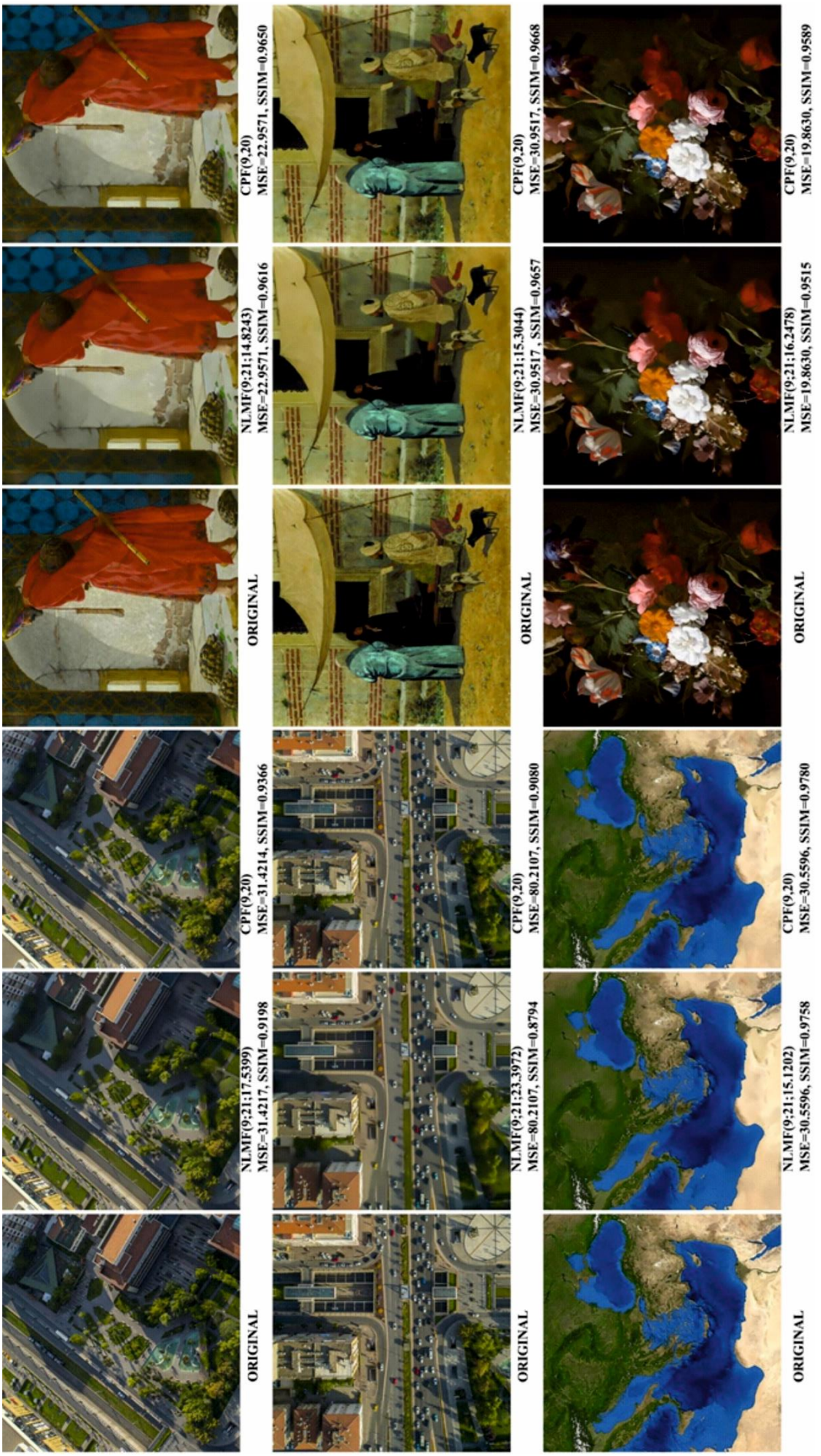

Figure 5. Comparison of CPF and NLMF for the same MSE values on Test Images (Please use zoom in to see details in the image)

MSE is a statistical measure that calculates the average of the squared differences between predicted and actual values. It is commonly used to evaluate the performance of regression models. The equation for MSE is given in Equation 3:

$$\mathrm{MSE} = \frac{1}{\mathrm{M} \cdot \mathrm{N}} \sum_{\mathrm{i}=1}^{\mathrm{M}} \sum_{\mathrm{j}=1}^{\mathrm{N}} \left(\mathrm{A}_{\mathrm{i,j}} - \mathrm{B}_{\mathrm{i,j}}\right)^2 \qquad (3)$$

where "M" and "N" denote the 2D image size in pixels, and "A" and "B" denote the original and the smoothed images, respectively.

SSIM is a metric used to measure the similarity between two images. It compares the structural information of the images, including luminance, contrast, and structure, to determine the similarity. SSIM values range from -1 to 1, with 1 indicating a perfect match between the images. The formulation of the SSIM is given in Equation 4.

$$\mathrm{SSIM} = \frac{\left(2\mu_x\mu_y + \mathrm{C}_1\right)\left(2\sigma_{xy} + \mathrm{C}_2\right)}{\left(\mu_x^2 + \mu_y^2 + \mathrm{C}_2\right)\left(\sigma_x^2 + \sigma_y^2 + \mathrm{C}_2\right)} \qquad (4)$$

μ_x: The pixel sample mean of *x*.
μ_y: the pixel sample mean of *y*.
σ_x^2: The variance of x.
σ_y^2: The variance of y.
σ_{xy}: The covariance of x and y.
$C_1=(k_1 \cdot L)^2$, $C_2=(k_2 \cdot L)^2$: two variables to stabilize the division with weak denominator;
L: the dynamic range of the pixel-values.
$k1 = 0.01 k2 = 0.03$

SSIM has valuable properties, including indiscernible identity and symmetry. It's not a distance function because it doesn't fulfil triangle inequality or non-negativity. Yet, it can transform into a normalized root MSE measure that works as a distance function under certain conditions. The function's square is locally convex and quasiconvex, allowing for optimization. Please see [41] for the meanings of the symbols used in Equation 4. The experimental results for the test images using CPF and NLMF are shown in Figure 5. Upon examining Figure 5, we can conclude that while both methods yield the same MSE value, NLMF produces results that are over-smoothed, leading to partial loss of detail. In contrast, CPF produces images that are relatively smoother and of higher quality as measured by SSIM values, compared to NLMF.

4. Results and Conclusion

In digital image processing, the accurate identification and analysis of objects depend significantly on the connectivity of pixels. This concept plays a vital role in object recognition and segmentation in various domains, such as medical imaging and video surveillance. Image smoothing also plays a crucial role in reducing noise and enhancing details, thereby improving the visual quality in applications such as medical imaging, video processing, and computer vision. Without considering the connectivity of pixels and employing image smoothing techniques, image processing tasks would be challenging and less reliable.

In this paper, a novel image smoothing filter based on gray connected pixels, termed CPF, is proposed. The experimental results demonstrate that CPF outperforms the widely used non-local means filter (NLMF) in terms of detail preservation while having the same mean square error (MSE) values. Thus, CPF can be considered as a valuable tool for various image processing applications.

Some advantages and disadvantages of the CPF are given below:

1. Since the structure of the CPF is very simple, it can be easily adapted to different applications.
2. CPF is a non-recursive, non-iterative and non-linear image smoothing method.
3. Smoothed images produced with CPF contain relatively more details.
4. The speed of CDF, like NLMF, is dependent on the sliding window size.

Author contributions

Erkan Beşdok: Data curation, Software, Validation. **Pınar Çivicioğlu:** Conceptualization, Methodology, Software, Writing, Editing

Conflicts of interest

The authors declare no conflicts of interest.

References

1. Perri, S., Spagnolo, F., & Corsonello, P. (2020). A parallel connected component labeling architecture for heterogeneous systems-on-chip. Electronics, 9(2), 292.
2. Chen, J., Nonaka, K., Sankoh, H., Watanabe, R., Sabirin, H., & Naito, S. (2018). Efficient parallel connected component labeling with a coarse-to-fine strategy. IEEE Access, 6, 55731-55740.
3. Narasimhan, R. S., Vengadarajan, A., & Ramakrishnan, K. R. (2017, March). Design of connected component analysis-based clustering of CFAR image in pulse Doppler radars. In 2017 IEEE Aerospace Conference (pp. 1-6). IEEE.
4. Civicioglu, P., & Alci, M. (2003, December). CCII based analog circuit for the edge detection of MRI images. In 2003 46th Midwest Symposium on Circuits and Systems (Vol. 1, pp. 341-344). IEEE.
5. Jeong, J. W., Lee, G. B., Lee, M. J., & Kim, J. G. (2016). A single-pass connected component labeler without label merging period. Journal of Signal Processing Systems, 84(2), 211-223.
6. Besdok, E. (2004). Impulsive noise suppression from images with a modified two-step iterative-median filter. Journal of Electronic Imaging, 13(4), 714-719.

7. Çivicioğlu, P., & Alçı, M. (2004). Edge detection of highly distorted images suffering from impulsive noise. AEU-International Journal of Electronics and Communications, 58(6), 413-419.
8. Wang, Y., & Bhattacharya, P. (1996). On parameter-dependent connected components of gray images. Pattern Recognition, 29(8), 1359-1368.
9. Beşdok, E., Çivicioğlu, P., & Alçı, M. (2004). Impulsive noise suppression from highly corrupted images by using resilient neural networks. In Artificial Intelligence and Soft Computing-ICAISC 2004: 7th International Conference, Zakopane, Poland, June 7-11, 2004. Proceedings 7 (pp. 670-675). Springer Berlin Heidelberg.
10. Wang, Y., & Bhattacharya, P. (1996, November). Gray connected components and image segmentation. In Applications of Digital Image Processing XIX (Vol. 2847, pp. 118-129). SPIE.
11. Donato, M., Hansen, K., Kalavakuru, P., Kirchgessner, M., Kuster, M., Porro, M., ... & Turcato, M. (2017). First functionality tests of a 64× 64 pixel DSSC sensor module connected to the complete ladder readout. Journal of Instrumentation, 12(03), C03025.
12. Tang, J. W., Shaikh-Husin, N., Sheikh, U. U., & Marsono, M. N. (2018). A linked list run-length-based single-pass connected component analysis for real-time embedded hardware. Journal of Real-Time Image Processing, 15, 197-215.
13. Ray, V., & Goyal, A. (2016, January). Image-based fuzzy c-means clustering and connected component labeling subsecond fast fully automatic complete cardiac cycle left ventricle segmentation in multi frame cardiac MRI images. In 2016 International Conference on Systems in Medicine and Biology (ICSMB) (pp. 36-40). IEEE.
14. Ito, Y., & Nakano, K. (2010). Low-latency connected component labeling using an FPGA. International Journal of Foundations of Computer Science, 21(03), 405-425.
15. Chang, W. Y., & Chiu, C. C. (2014, June). Directional Connected Components Algorithm Based on Gradient Information. In 2014 International Symposium on Computer, Consumer and Control (pp. 280-283). IEEE.
16. Beşdok, E., & Yüksel, M. E. (2005). Impulsive noise suppression from images with Jarque-Bera test based median filter. AEU-International Journal of Electronics and Communications, 59(2), 105-110.
17. Çivicioğlu, P., Alçı, M., & Beşdok, E. (2004). Impulsive noise suppression from images with the noise exclusive filter. EURASIP Journal on Advances in Signal Processing, 2004(16), 2434-2440
18. Yeong, L. S., Ang, L. M., & Seng, K. P. (2010, July). Efficient connected component labelling using multiple-bank memory storage. In 2010 3rd International Conference on Computer Science and Information Technology (Vol. 9, pp. 75-79). IEEE.
19. Gunen, M. A., Civicioglu, P., & Beşdok, E. (2016). Differential search algorithm-based edge detection. The International Archives of Photogrammetry, Remote Sensing and Spatial Information Sciences, 41(B7), 667-670
20. Bieniek, A., & Moga, A. (1998). A connected component approach to the watershed segmentation. Computational Imaging and Vision, 12, 215-222.
21. Sun, Y., Sun, C., & Wang, W. (2000, August). Color images segmentation using new definition of connected components. In WCC 2000-ICSP 2000. 2000 5th International Conference on Signal Processing Proceedings. 16th World Computer Congress 2000 (Vol. 2, pp. 863-868). IEEE.
22. Ma, D., Liu, S., & Liao, Q. (2017). Run-based connected components labeling using double-row scan. In Image and Graphics: 9th International Conference, ICIG 2017, Shanghai, China, September 13-15, 2017, Revised Selected Papers, Part III 9 (pp. 264-274). Springer International Publishing.
23. Asano, T. (2012). In-place algorithm for erasing a connected component in a binary image. Theory of Computing Systems, 50(1), 111-123.
24. Bekhtin, Y. S., Gurov, V. S., & Zavalishin, S. S. (2015, June). A run equivalence algorithm for parallel connected component labeling on CPU. In 2015 4th Mediterranean Conference on Embedded Computing (MECO) (pp. 276-279). IEEE.
25. Yunfeng, G., Feiyang, W., & Xiaotian, H. (2014, August). Connected components labeling algorithm based on run-length table searching. In 2014 9th International Conference on Computer Science & Education (pp. 700-704). IEEE.
26. Rasmusson, A., Sørensen, T. S., & Ziegler, G. (2013). Connected components labeling on the GPU with generalization to voronoi diagrams and signed distance fields. In Advances in Visual Computing: 9th International Symposium, ISVC 2013, Rethymnon, Crete, Greece, July 29-31, 2013. Proceedings, Part I 9 (pp. 206-215). Springer Berlin Heidelberg.
27. Il, H. J., Kim, H. K., & Oh, W. G. (2015, January). Fast text line detection by finding linear connected components on Canny edge image. In 2015 21st Korea-Japan Joint Workshop on Frontiers of Computer Vision (FCV) (pp. 1-4). IEEE.
28. Kowalczyk, M., & Kryjak, T. (2021, September). A Connected Component Labelling algorithm for a multi-pixel per clock cycle video stream. In 2021 24th Euromicro Conference on Digital System Design (DSD) (pp. 43-50). IEEE.
29. Rouabeh, H., Abdelmoula, C., & Masmoudi, M. (2016, December). A new efficient connected component labeling algorithm and its VHDL circuit. In 2016 28th International Conference on Microelectronics (ICM) (pp. 105-108). IEEE.
30. Bailey, D. G. (2020, November). History and evolution of single pass connected component analysis. In 2020 35th International Conference on Image and Vision Computing New Zealand (IVCNZ) (pp. 1-6). IEEE.
31. Wang, Y., & Bhattacharya, P. (1996, October). Image analysis and segmentation using gray connected components. In 1996 IEEE International Conference on Systems, Man and Cybernetics. Information Intelligence and Systems (Cat. No. 96CH35929) (Vol. 1, pp. 444-449). IEEE.
32. Kang, S. M., Kim, J. H., Yuan, Z., Song, S. H., & Cho, J. D. (2014, June). A fast region expansion labeling of

connected components in binary image. In The 18th IEEE International Symposium on Consumer Electronics (ISCE 2014) (pp. 1-2). IEEE.
33. Flatt, H., Blume, S., Hesselbarth, S., Schunemann, T., & Pirsch, P. (2008, July). A parallel hardware architecture for connected component labeling based on fast label merging. In 2008 International Conference on Application-Specific Systems, Architectures and Processors (pp. 144-149). IEEE.
34. Krämer, M., Afzal, M. Z., Bukhari, S. S., Shafait, F., & Breuel, T. M. (2012, November). Robust stereo correspondence for documents by matching connected components of text-lines with dynamic programming. In Proceedings of the 21st International Conference on Pattern Recognition (ICPR2012) (pp. 734-737). IEEE.
35. Yapa, R. D., & Koichi, H. (2007, March). A connected component labeling algorithm for grayscale images and application of the algorithm on mammograms. In Proceedings of the 2007 ACM symposium on Applied computing (pp. 146-152).
36. Zhang, D., Ma, H., & Pan, L. (2019). A gamma-signal-regulated connected components labeling algorithm. Pattern Recognition, 91, 281-290.
37. Shim, J., Yoon, M., & Lee, Y. (2019). Feasibility of fast non local means filter in pediatric chest x-ray for increasing of pulmonary nodule detectability with 3D printed lung nodule phantom. Journal of Radiological Protection, 39(3), 872-889
38. Shim, J., Yoon, M., & Lee, Y. (2018). Feasibility of newly designed fast non local means (FNLM)-based noise reduction filter for X-ray imaging: A simulation study. Optik, 160, 124-130.
39. Civicioglu, P., & Besdok, E. (2019). Bernstain-search differential evolution algorithm for numerical function optimization. Expert Systems with Applications, 138, 112831.
40. Perona, P., & Malik, J. (1990). Scale-space and edge detection using anisotropic diffusion. IEEE Transactions on pattern analysis and machine intelligence, 12(7), 629-639.
41. Civicioglu, P., & Besdok, E. (2022). Contrast stretching based pansharpening by using weighted differential evolution algorithm. Expert Systems with Applications, 208, 118144.

Mersin Photogrammetry Journal
https://dergipark.org.tr/en/pub/mephoj
e-ISSN 2687-654X

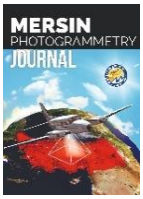

Deterioration analysis of historical village house structure in Mersin Kanlıdivane archaeological area by UAV method

Lale Karataş*[1], Murat Dal[2]

[1]*Mardin Artuklu University, Department of Architecture and Urban Planning, Türkiye*
[2]*Munzur University, Department of Architecture, Türkiye*

Keywords
UAV
Remote Sensing
Photogrammetry
Cultural Heritage

Research Article
DOI:10.53093/mephoj.1290231

Received:30.04.2023
Revised:17.05.2023
Accepted:19.05.2023
Published:27.05.2023

Abstract

The village house located in the Mersin Kanlıdivane archaeological site is one of the oldest settlements in the ruins, built in the second century. The house is mainly built of a yellowish beige limestone. This stone, which is the main material of the building, shows many deterioration patterns today. The aim of the study is to determine the dominant deterioration pattern of the stones in the village house structure in the Mersin Kanlıdivane archaeological site and to investigate the source of the deterioration. In order to investigate the deterioration patterns in the structure, the images obtained by UAV photogrammetry were interpreted and the types of deterioration were mapped. In the study, it is seen that even the types of material problems based on the smallest detail can be determined based on virtual visual inspection, thanks to UAV photogrammetry, without observing the structure in situ with UAV photogrammetry. The findings obtained in the study shows that the color change and surface loss deterioration on the stone surfaces has reached advanced levels as a result of the structure's exposure to the strong climate-induced sun and water effects for centuries. The results of the study show that the main damage observed on the stone surface of the structure is caused by the erosion by the effect of water. Restoration methods should be tried to stabilize the deterioration and replace the most degraded stones. It is recommended to use water-repellent surface coatings to protect the natural stone, especially against the intense water effect in the building.

1. Introduction

Natural stone is one of the oldest building materials. The majority of cultural heritage structures in the world, such as the Ancient City of Petra in Jordan, the Temples of Luxor in Egypt, the Ancient City of Nimrud in Iraq, are made of stone. Historical stone structures are important in terms of reaching values such as the living spaces, aesthetic concerns and beliefs of past societies to the present. However, these cultural heritage values are threatened by various deterioration processes due to natural or anthropogenic reasons [1].

Water-related damages are reported as the most common problems affecting stone monuments in the world. Various findings have been obtained in many studies on the corrosive effects of rainwater. A study conducted on sandstone material by [2] was reported that pitting formed in the stone material in contact with rain water. Bonazza et al. [3] reported that rainwater has a corrosive effect even at low exposures, especially on carbonated stones. Gulotta et al., [4] reported that there is intense erosion on the marble in the parts exposed to atmospheric water. Winkler [5] reported that the facade walls exposed to rain water in marble and limestones occured significant erosion, while the facade walls on the protected side were less damaged. In addition, it has been emphasized by many studies that long term effect of stone material with water causes erosion, especially in architectural structures such as fountains built of carbonate stone [6-8]. Germinario et al. [9] reported that the siltstone material can be completely disintegrated by the action of water. In addition, it has been reported that the stone has got colour of change when stones exposed to water long terms [10-13]. Gulotta et al. [14] reported that the water effect causes as spalling, fragmentations, pitting due to the structure of the minerals in the serpentinite stone.

* **Corresponding Author**

*(karataslale@gmail.com) ORCID ID 0000-0001-8582-4612
(muratdal@munzur.edu.tr) ORCID ID 0000-0001-5330-1868

Cite this article

Karataş, L., & Dal, M. (2023). Deterioration analysis of historical village house structure in Mersin Kanlıdivane archaeological area by UAV method. Mersin Photogrammetry Journal, 5(1), 32-41

Other situations in the literature caused by the effect of water were reported as mass loss problems in stones exposed to cycles simulating sunlight, evaporation, condensation [15-23]. Lubera [24] reported six stone types (fine-grained conglomerate, breccia, limestone, sandstone, amphibolite, and two granites) in the study, with the effect of water about 6% in breccia samples, 0.5% in limestone and 4% in fine-grained conglomerate samples. The study reported that there was a mass loss below 0.3% in other samples. In addition, the various studies is emphasized that the acidity of water tends to increase over time due to atmospheric pollutants in stone structures, which further increases erosion in stones [25-26].

In order to ensure the sustainability of the buildings, the deterioration of the stone structures should be documented firstly. Conservation recommendations should be made by experts with reference to correct documentation. Nowadays, modern technologies should be used in documentary works which made by architects [27-29]. Different methods are used in order to be documented, protected and introduced of these monuments [30-31]. Today, technologies such as photogrammetry and laser scanning techniques are used to document the material problems of a cultural heritage property. The use of three-dimensional visualization techniques is also becoming more popular day by day. Laser scanning is an object-contact technology that digitally captures the shape of physical objects using laser light. 3D laser scanners collect "point clouds" as data from the surface of an object [32-34]. These techniques provide more realistic visualizations than graphic-based object models [35-38]. In addition, the use of Unmanned Aerial Vehicles (UAV) provides great convenience for documenting material deterioration problems. Unmanned aerial vehicle is a very useful tool for documenting the structure and material problems without touching the object [39-42].

UAVs have become more accessible to individual users due to their low cost, flexibility, ease of use and readiness for implementation [43-45]. The use of UAVs in cultural heritage studies is becoming more and more common. It enables fast, accurate and low-cost data collection, especially in areas where access to structures is difficult [46]. In the literature studies conducted to evaluate material damage by using unmanned aerial vehicles (UAV) reported that the benefits of unmanned aerial vehicles (UAVs) in identifying material deterioration in structures [47-50]. Pepi et al. [51] investigated the material deterioration of a stone bridge by UAV and photogrammetric methods. The study reported that damage can be detected quickly from the images obtained. Material deterioration such as cracks, microcracks, material loss problems can be easily documented and mapped by this method. In addition, the results of the study emphasized that the method provides significant advantages by reducing time for documantation. Duque et al. [52] conducted a study using UAV for damage assessment (crack lengths, thicknesses, and rust-stained areas) of a wooden bridge in South Dakota. In the results of the study stated that high quality images were obtained to measure bridge damage. In addition, damage level classification based on the UAV image can be created based on the damage levels wiht the details in the images obtained. Khaloo et al. [49] used UAV to observe the damage in a bridge and reported that missing bolts, damaged beam connections and defective beams could be detected from the data obtained from the results. In addition, the reported that damages can be detected in a shorter time and without the risk of injury compared to the traditional method. Kim et al. [50] reported that they were able to measure concrete cracks from images captured by a UAV, and the method gave accurate results for cracks with a thickness greater than 0.1 mm. Harrington [53] reported that sufficient high-quality images can be obtained from the images obtained by UAV in damage detection. The study reported that these data can be used for crack length, thickness and rust-stained area measurements and the UAV-image-based method reduces time, expense and safety risk.

In summary, several studies have reported that UAVs have many potential benefits in detecting material problems. The aim of the study is to determine the problems of the stone material in a historical village house in Mersin Kanlıdivane archaeological site. The village house located in the Mersin Kanlıdivane archaeological area, which is the subject of the study, was built in the second century. It is one of the oldest settlements in the ruins. The house was built from a yellowish beige limestone. This stone, which is the main material of the building, shows many deterioration patterns today. In order to investigate the deterioration patterns in the structure, the images obtained by UAV photogrammetry were interpreted and the types of deterioration were mapped. In the study confirmed that even the smallest detail-based material problems can be detected, based only on virtual visual inspection, by using UAV.

In this context, the location and history of the building were explained first. In the next stage, UAV researches for the determination of material problems are included. In the next stage, the findings are explained and in the conclusion section, conservation suggestions are presented for the detected deteriorations.

2. Material and Method

2.1. Study area

Kanytella, which remained within the borders of Rough Cilicia in Antiquity, is known by its current name as Bloody Divane. The area is one of the largest archaeological sites in Mersin [54]. The ruins of Kanlıdivane consist of a sinkhole that is widely seen and believed to be sacred around Mersin and Silifke, and religious places, houses, roads, olive oil production workshops, cisterns, tower and necropolis around it. The settlement activities, which started from the Hellenistic Period (3rd century BC), continued uninterruptedly until the Late Antiquity (7th century AD). The village house, which was examined as a case study in the study, is located in the Mersin Kanlıdivane archaeological area. The building is dated to the 2nd century AD, based on other structures in the archaeological area. Thanks to its building architecture, it is only the most magnificent house of the archaeological site. Like other structures in

the area, the village house was built mainly with yellowish-beige limestone. Currently, this stone shows many deterioration features in all structures in the area, especially in this structure [55] (Figure 1). Therefore, the main purpose of our research is to determine the main weathering patterns of the limestone used in the field and to investigate the causes of its deterioration. For this purpose, UAV photogrammetric survey of the village house was conducted. The data obtained were interpreted and analyzed. The results of field and descriptive analysis studies are given in the findings.

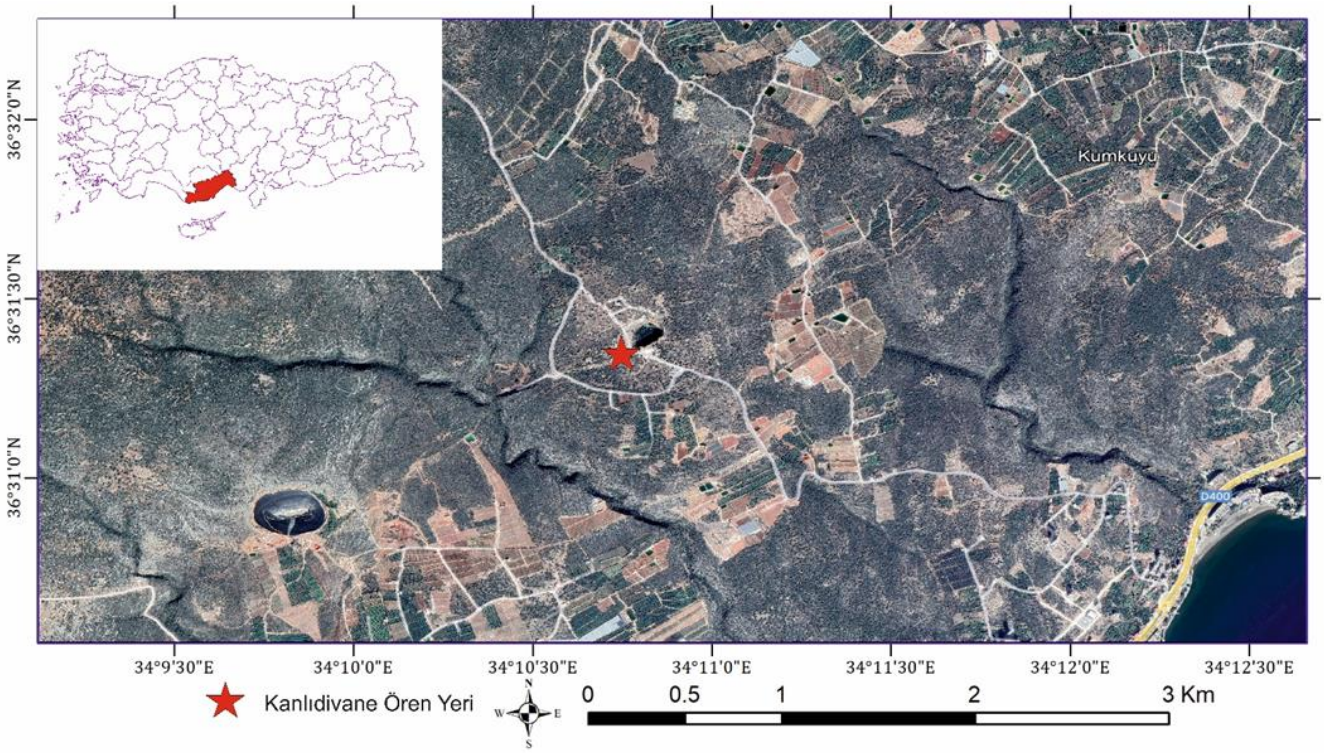

Figure 1. The location of the historical village house in the archaeological site

This study consists of two stages: field and office work. The phases of on-site examination of the study area, photographing and taking images of the mausoleum with an unmanned aerial vehicle constitute the field study phase. During the office work phase, the data taken from the unmanned aerial vehicle was transferred to the computer environment, interpreted and processed. The images collected in the field by the UAV method were transferred to the computer in the office environment. The types of material degradation from the images obtained were defined using the illustrated dictionary published by ICOMOS [56].

Identified material deteriorations were mapped by dividing them into classes on the basis of stone structural elements in masonry structures. In the literature, the structural elements seen in masonry structures are defined as vertical carriers, horizontal carriers, stairs, wall cavities and auxiliary elements [57]. Vertical carriers in the building are defined as pillars, columns and walls. There is no use of pillars or columns in the building. Horizontal carriers from the building elements are defined as floors. Flat flooring is used in the building. The auxiliary elements in the structure are; gargoyles are defined as ornaments and moldings.

2.2. UAV photogrammetry

UAV is a platform that can fly manually or autonomously without the need for a pilot. It has been frequently used in various engineering projects in recent years. landslide modeling, landslide inventory map creation [58], shoreline determination [59], pond volume determination [60], historical monument modeling [61], degradation of historical buildings [62], settlement modeling and discordance plane extraction [63] has been successfully applied in their projects. By using the UAV can obtain data without touching the object. This ensures that the original state of the object or land remains intact [64]. Through the datas can be seen the current state of the land or an object with high sensitivity and resolution [65-67].

2.3. Fieldwork

At this stage of the study, necessary permissions were obtained to fly in the Kanlıdivane region, which is the study area. Then, the flight altitudes at which the images will be taken around the grave were determined. Images were captured manually with the Parrot Anafi HDR Drone (Figure 2). Its technical specifications are shown in Table 1.

Every detail of the structure was tried to be captured by flying first at low altitude and then at high altitude. The lower the flight, the clearer the image will be [68]. A total of 101 photos were taken. The camera was calibrated beforehand and no changes were made in the parameters. A smartphone was used together with the remote control during the photo shoot. Free Flight 6 and Pix4D Capture applications have been installed in order for the smartphone and the remote to work integrated.

Figure 2. Anafi Parrot

Table 1. Technical properties of Anafi

Feature	Numeric value
Controller weight	386 g
Battery weight	126 g
Number of batteries	4
Max. horizontal speed	15.2 m/s
Max. vertical speed	4 m/s
Flight time	25 min
Max. wind resistance	13.9 m/s
Max. distance	4000 m
Operating temperature	-10…40 C°

2.4. Office-work

After the completion of the image acquisition within the scope of the field work, the office work phase was started. First of all, the data obtained from the field were transferred to the computer environment. Data processing was done in Agisoft Metashape program. The office work, which started after half a day of field work, was completed in one day. All the photos taken were used in the documentation process.

3. Results

3.1. Deterioration in vertical carriers

In the literature, vertical carriers of building elements in masonry structures are defined as feet, columns and walls. There is no use of pillars or columns in the building. The deteriorations seen in the walls in the building were determined as change of colur, surface loss and pollution of surface. Change of colour due to water effect was observed in the parts close to the ground on the south façade of the building. On the upper parts of the façade, pollution of surface, which is a gray dirt layer formed on the stone as a result of the air pollutants created by the fires in the environment, can be seen (Figure 3).

Figure 3. Change of color on the south facade (a), contamination of surface (b), contamination surface (c)

There is a gargoyle on the northern façade of the building. This gargoyle is the system that collects the rain water reaching the structure and removes it from the structure. Since the sunbathing time is shorter on this facade of the building compared to the other facades, the rain water that comes into contact with this facade remains in the inner body of the stone for a longer time without evaporation. For this reason, the color change in the structure of the stone caused by rain water on this facade is more than the other facades, and it formed as an orangish color (Figure 4).

Change of color and contamination of surface material problems were encountered on the western façade of the building (Figure 5).

Pollution of surface was detected on the eastern façade of the building (Figure 6).

(a) (b) (c)

Figure 4. Stone material problems on the north facade: a) pitting, b) change of color c) contamination of surface

Figure 5. Change of color on the west facade (a), surface contamination (b)

Figure 6. Pollution of surface

3.2. Deterioration in horizontal carriers

In the literature, horizontal carriers from building elements in masonry structures are defined as floors. Flat flooring is used in the building. There is no deterioration in the flat floor (Figure 7).

Figure 7. The flat floor seen in the building

3.3. Deterioration in auxiliary elements

In the literature, auxiliary elements of building elements in masonry structures; gutters are defined as ornaments and moldings. There is surface loss in the gutters seen on the facade of the building (Figure 8).

Figure 8. Surface loss in gutters in the structure

4. Discussion

The main purpose of the study is to determine the deterioration patterns of the stones in the historical village house in the Mersin Kanlıdivane archaeological area and to investigate the source of the deterioration. In order to investigate the deterioration patterns in the structure, the images obtained by UAV photogrammetry were interpreted and the types of deterioration were mapped. The research conducted in the historical village house with UAV photogrammetry enabled many images with high resolution to be taken, including orthophotos of the plans and façades of the building. With the UAV photogrammetry method, it was possible to detect even the types of material problems based on the smallest detail, based only on virtual visual inspection, without an on-site observation of the structure. The results shows that the damage can be detected quickly based on the visual inspection of the images obtained using UAVs. It has been determined that the deteriorations can be mapped using these images and the method used provides significant advantages in the detection of material deterioration by reducing the working time [49,51].

Another important finding is that material problems detected in the maps produced from the data obtained from the UAV method in the structure is change of color, surface loss and surface contamination. Change of color was detected in a large part of the structure. There is a gutter on the north façade of the building. The water accumulated by the rain in the structure is removed from this gutter. It is understood that the water flowing from the gutters rises from the ground and enters the interior of the body walls. For this reason, it is seen that the change of color decay patterns occurs more on the stones in contact with the ground and on the northwest sides compared to protected area from the sun. This finding supports studies stating that stones exposed to water change of color due to various external factors or the structure of the stone [9-13, 69].

On the east and west surfaces exposed to strong winds, mainly stone material occurs damage. It is seen that the change of colour problem, which is advanced on all façades, is more common on the south façade. It is predicted that this situation is due to the long sunbathing period on the south façade. The rapid evaporation of the water entering the inner surface of the wall caused color changes due to the structure of the stone. Winkler [5] supports that the exposed side of the limestones shows significant erosion, while the erosion occurs less on the protected side. For this reason, there are problems related to the corrosive effects of water, especially on the north facade. This finding supports studies that indicate erosion in stones exposed to water [3,14,70].

In addition, the water flowing from the gutters on the north façade caused pitting problems by damaging the stone material at the points of direct contact on the façade. Waragai & Hiki [70] confirms the phenomenon of pitting in stone materials in direct contact with water, which they obtained in their study results. The results confirm the findings of various studies that the stone material causes erosion, especially in fountains built of carbonate stone, as a result of constant contact with running water [6-8].

Another result is that the gray layer, which is seen in the form of surface pollution on the facades, may be caused by the fires that people set to clean the bushes. It is known that the residents of the area carried out stubble burning in order to clear the bushes around the building. This situation caused the formation of a gray layer on the walls of the building. It is remarkable that the gray layer is excessive on the façades except the south façade, where the water stays on the wall for a long time. This situation shows that the water evaporates faster from the wall of the building due to the sunshine duration on the south façade, causing a change of color. On the north façade, as the water stays in contact with the body

wall more and evaporates slowly, the black layer caused by the fire smoke on the façade is less cleaned and forms a crust. This determination was made by de Azcona et al. [25] support the fact that the acidity of water tends to increase over time due to the atmospheric pollutants obtained in the results of the study, which further increases the erosion and change of colour in the stones.

Another important finding is that the gray layer seen in the form of surface pollution on the facades is thought to be caused by the fires that people lit to clear the bushes. It is known that the residents of the area carried out stubble burning in order to clear the bushes around the building. This situation caused the formation of a gray layer on the body walls of the building. It is remarkable that the gray layer is excessive on the façades except the south façade, where the water stays on the wall for a long time. Based on this situation, it is predicted that due to the sunshine duration on the south façade, the water evaporates faster from the wall of the building and causes a color change in this situation. On the north façade, the water stays in contact with the wall more. In this case, the fact that the water evaporates more slowly from this façade is less able to clean the black layer caused by the fire fumes on the façade and forms black crusts. This determination was made by de Azcona et al. [25], the fact that the acidity of water tends to increase over time due to atmospheric pollutants, which further increases the erosion and discoloration of stones.

5. Conclusion

In the study presented, UAV photogrammetry was used to investigate the stone decay patterns of the village house, which is a historical masonry building in Kanlı Divane, one of the largest archaeological sites in Mersin, and the deterioration types were mapped by interpreting the images obtained. The results shows that the main damage observed on the stone surface of the structure is due to the erosion by the effect of water. It is seen that the change of color and surface loss decay types on the stone surfaces have reached advanced levels as a result of exposure to the strong climate-induced sun and water effects for centuries. Restoration methods should be tried to stabilize the deterioration and replace the most damaged stones.

To clean surface pollution deterioration, to increase the stone's resistance to environmental pollution and to prevent subsequent exposure to weathering, treatment should be considered. Firstly, stubble burning processes in the environment, which will eliminate the main reason for this process, should be prohibited and prevented.

In addition, in this study, it is important to create a database containing the hydromechanical and thermal properties of limestone in order to protect the village house and other structures in the Kanlıdivane archaeological site area. Given ICOMOS code principles such as compatibility, reversibility and durability, these data can be used as a reference level to define requirements for the selection of restoration materials, mortars, replacement stones, surface protection and reinforcement products. Secondly, it is recommended to replace the deteriorated masonry stones to decontaminate and consolidate the affected stones. Third, a systematic approach should be taken to select suitable raw materials for the formulation of compatible and durable repair and cleaning materials. The properties of the materials (especially new materials) used in restoration works and their compatibility with existing materials should be determined exactly. This should include long-term effects to avoid unwanted side effects.

In addition, it is recommended to prepare a research plan that includes one-year monitoring of the microclimate, as well as tests and analyzes on the stone, in order to determine the damage process in the structure and to establish a solid foundation for the preservation of the structure. First of all, the stone type should be determined by macroscopic features and thin section microscopy, and the moisture distribution in the structure should be determined gravimetrically on samples taken at different heights and depths. The content and type of salt in the building stone should be determined by X-ray diffraction and ion chromatography [71].

Acknowledgement

We would like to thank the institutions that gave permission for the drone flight

Author contributions

Lale Karataş: Conceptualization, Methodology, Software, Writing-Original draft preparation **Murat Dal:** Data curation, Writing-Reviewing and Editing.

Conflicts of interest

The authors declare no conflicts of interest.

References

1. Hatır, E., Korkanç, M., Schachner, A., & İnce, İ. (2021). The deep learning method applied to the detection and mapping of stone deterioration in open-air sanctuaries of the Hittite period in Anatolia. Journal of Cultural Heritage, 51, 37-49.
2. Waragai, T., & Hiki, Y. (2019). Influence of microclimate on the directional dependence of sandstone pillar weathering in Angkor Wat temple, Cambodia. Progress in Earth and Planetary Science, 6(1), 1-14.
3. Bonazza, A., Vidorni, G., Natali, I., Ciantelli, C., Giosuè, C., & Tittarelli, F. (2017). Durability assessment to environmental impact of nano-structured consolidants on Carrara marble by field exposure tests. Science of the Total Environment, 575, 23-32.
4. Gulotta, D., Villa, F., Cappitelli, F., & Toniolo, L. (2018). Biofilm colonization of metamorphic lithotypes of a renaissance cathedral exposed to urban atmosphere. Science of the Total Environment, 639, 1480-1490.
5. Winkler, E. (1997). Stone in architecture: properties, durability. Springer Science & Business Media.

6. Bello, M. A., Martin, L., & Martin, A. (1992). Decay and treatment of macael white marble. Studies in conservation, 37(3), 193-200.
7. Sarró, M. I., García, A. M., Rivalta, V. M., Moreno, D. A., & Arroyo, I. (2006). Biodeterioration of the lions fountain at the Alhambra Palace, Granada (Spain). Building and Environment, 41(12), 1811-1820.
8. Sanjurjo-Sánchez, J., & Alves, C. (2012). Decay effects of pollutants on stony materials in the built environment. Environmental Chemistry Letters, 10, 131-143.
9. Germinario, L., Oguchi, C. T., Tamura, Y., Ahn, S., & Ogawa, M. (2020). Taya Caves, a Buddhist marvel hidden in underground Japan: stone properties, deterioration, and environmental setting. Heritage Science, 8(1), 1-20.
10. Ďoubal, J. (2017). The restoration of the Stone Fountain in Kutná Hora: An assessment of the contemporary intervention within the context of repairs throughout history. Studies in Conservation, 62(7), 371-383.
11. Dreesen, R., Nielsen, P., & Lagrou, D. (2007). The staining of blue stone limestones petrographically unraveled. Materials Characterization, 58(11-12), 1070-1081.
12. Zha, J., Wei, S., Wang, C., Li, Z., Cai, Y., & Ma, Q. (2020). Weathering mechanism of red discolorations on Limestone object: a case study from Lingyan Temple, Jinan, Shandong Province, China. Heritage Science, 8(1), 1-12.
13. Germinario, L., Siegesmund, S., Maritan, L., Simon, K., & Mazzoli, C. (2017). Trachyte weathering in the urban built environment related to air quality. Heritage Science, 5(1), 1-17.
14. Gulotta, D., Bontempi, E., Bugini, R., Goidanich, S., & Toniolo, L. (2017). The deterioration of metamorphic serpentinites used in historical architecture under atmospheric conditions. Quarterly Journal of Engineering Geology and Hydrogeology, 50(4), 402-411.
15. Hall, K., & Hall, A. (1996). Weathering by wetting and drying: some experimental results. Earth Surface Processes and Landforms, 21(4), 365-376.
16. Trenhaile, A. (2006). Tidal wetting and drying on shore platforms: an experimental study of surface expansion and contraction. Geomorphology, 76(3-4), 316-331.
17. Mottershead, D. N. (1982). Rapid weathering of greenschist by coastal salt spray, East Prawle, south Devon: a preliminary report. Proceedings of the USSHER Society, 5(3), 347-353.
18. Aly, N., Hamed, A., & Abd El-Al, A. (2020). The impact of hydric swelling on the mechanical behavior of Egyptian Helwan limestone. Periodica Polytechnica Civil Engineering, 64(2), 589-596.
19. Iucolano, F., Colella, A., Liguori, B., & Calcaterra, D. (2019). Suitability of silica nanoparticles for tuff consolidation. Construction and Building Materials, 202, 73-81.
20. Dursun, F., & Topal, T. (2019). Durability assessment of the basalts used in the Diyarbakır City Walls, Turkey. Environmental Earth Sciences, 78(15), 1-24.
21. Noor-E-Khuda, S., & Albermani, F. (2019). Flexural strength of weathered granites under wetting-drying cycles: implications to steel structures. Advanced Steel Construction, 15(3), 225-231.
22. Pozo-Antonio, J., & Alonso-Villar, E. (2020). Stone durabılıty of a surfactant-synthesısed alkosylane consolıdant on granıtes wıth dıfferent mıneralogy and texture. Egyptian Journal of Archaeological and Restoration Studies, 10(2), 153-164.
23. Bustamante Montoro, R., Vazquez, P., Rodríguez Monteverde Cantarell, P., & Monjo Carrió, J. (2020). Adapted ageing tests for the evaluation of alabaster used in the restoration of Bishop's Palace of Tarazona. Materiales de Construcción, 70(338), e219-e231.
24. Lubera, E. (2014). Frost weathering of selected rocks from the tatra mountains. Quaestiones Geographicae, 33(1), 75-88.
25. De Azcona, M. L., Gonzalez, R. F., & Martin, F. M. (2002). La conservación de los materiales pétreos en la Fuente de Cibeles, Madrid (España) Conservation of the stone in Cibeles Fountain, Madrid (Spain). Materiales de Construcción, 52(265), 65.
26. Karataş, L., Alptekin, A., Kanun, E., & Yakar, M. (2022). Tarihi kârgir yapılarda taş malzeme bozulmalarının İHA fotogrametrisi kullanarak tespiti ve belgelenmesi: Mersin Kanlıdivane ören yeri vaka çalışması. İçel Dergisi, 2(2), 41-49.
27. Mohammed, O., & Yakar, M. (2016). Yersel Fotogrametrik Yöntem ile İbadethanelerin Modellenmesi. Selcuk University Journal of Engineering Sciences, 15(2), 85-95.
28. Yakar, M., & Doğan, Y. (2017). Mersin Silifke Mezgit Kale Anıt Mezarı fotogrametrik rölöve alımı ve üç boyutlu modelleme çalışması. Geomatik, 2(1), 11-17.
29. Alyılmaz, C., Yakar, M., & Yılmaz, H. M. (2010). Drawing of petroglyphs in Mongolia by close range photogrammetry. Scientific Research and Essays, 5(11), 1216-1222.
30. Korumaz, A. G., Dülgerler, O. N., & Yakar, M. (2011). Kültürel mirasin belgelenmesinde dijital yaklaşimlar. Selçuk Üniversitesi Mühendislik, Bilim ve Teknoloji Dergisi, 26(3), 67-83.
31. Yakar, M., Toprak, A. S., Ulvi, A., & Uysal, M. (2015). Konya Beyşehir Bezariye Hanının (Bedesten) İha İle Fotogrametrik Teknik Kullanılarak Üç Boyutlu Modellenmesi. Türkiye Harita Bilimsel Ve Teknik Kurultayı, 25, 28.
32. Alptekin, A., & Yakar, M. (2021). 3D model of Üçayak Ruins obtained from point clouds. Mersin Photogrammetry Journal, 3(2), 37-40.
33. Karataş, L. (2023). 3D Laser Scanning and Photogrammetric Measurements for Documentation of the Facades of Mardin Castle, Türkiye. Advanced LiDAR, 3(1), 10-21.
34. Karataş, L., Alptekin, A., & Yakar, M. (2023). Investigating the limestone quarries as geoheritage sites: Case of Mardin ancient quarry. Open Geosciences, 15(1), 20220473.
35. Alyilmaz, C., Alyilmaz, S., & Yakar, M. (2010). Measurement of petroglyhps (rock of arts) of Qobustan with close range photogrammetry. International Archives of Photogrammetry, Remote

Sensing and Spatial Information Sciences, 38(Part 5), 29-32.
36. Unal, M., Yakar, M., & Yildiz, F. (2004, July). Discontinuity surface roughness measurement techniques and the evaluation of digital photogrammetric method. In Proceedings of the 20th international congress for photogrammetry and remote sensing, ISPRS (Vol. 1103, p. 1108).
37. Doğan, Y., & Yakar, M. (2018). GIS and three-dimensional modeling for cultural heritages. International Journal of Engineering and Geosciences, 3(2), 50-55.
38. Korumaz, A. G., Dülgerler, O. N., & Yakar, M. (2011). Kültürel mirasin belgelenmesinde dijital yaklaşimlar. Selçuk Üniversitesi Mühendislik, Bilim ve Teknoloji Dergisi, 26(3), 67-83
39. Kanun, E., Alptekin, A., & Yakar, M. (2021). Cultural heritage modelling using UAV photogrammetric methods: a case study of Kanlıdivane archeological site. Advanced UAV, 1(1), 24-33.
40. Mirdan, O., & Yakar, M. (2017). Tarihi eserlerin İnsansız Hava Aracı ile modellenmesinde karşılaşılan sorunlar. Geomatik, 2(3), 118-125.
41. Karataş, L., & Alptekin, A. (2022). Kagir Yapılardaki Taş Malzeme Bozulmalarının Lidar Tarama Yöntemi ile Belgelenmesi: Geleneksel Silvan Konağı Vaka Çalışması. Türkiye Lidar Dergisi, 4(2), 71-84
42. Alptekin, A., & Yakar, M. (2020). Mersin Akyar Falezi'nin 3B modeli. Türkiye Lidar Dergisi, 2(1), 5-9.
43. Karachaliou, E., Georgiou, E., Psaltis, D., & Stylianidis, E. (2019). UAV for mapping historic buildings: From 3D modelling to BIM. The International Archives of Photogrammetry, Remote Sensing and Spatial Information Sciences, 42, 397-402.
44. Caprioli, M., Mancini, F., Mazzone, F., Scarano, M., & Trizzino, R. (2015). UAV surveys for representing and document the cultural heritage. In Heritage and Technology, Mind Knowledge Experience, 56, 475-482
45. Karataş, L., Alptekin, A., & Yakar, M. (2022). Detection and documentation of stone material deterioration in historical masonry structures using UAV photogrammetry: A case study of Mersin Aba Mausoleum. Advanced UAV, 2(2), 51-64.
46. Stathopoulou, E. K., Georgopoulos, A., Panagiotopoulos, G., & Kaliampakos, D. (2015). Crowdsourcing Lost Cultural Herıtage. ISPRS Annals of Photogrammetry, Remote Sensing & Spatial Information Sciences, 2(5), 295
47. Ellenberg, A., Kontsos, A., Moon, F., & Bartoli, I. (2016). Bridge related damage quantification using unmanned aerial vehicle imagery. Structural Control and Health Monitoring, 23(9), 1168-1179.
48. Elmeseiry, N., Alshaer, N., & Ismail, T. (2021). A detailed survey and future directions of unmanned aerial vehicles (uavs) with potential applications. Aerospace, 8(12), 363.
49. Khaloo, A., Lattanzi, D., Cunningham, K., Dell'Andrea, R., & Riley, M. (2018). Unmanned aerial vehicle inspection of the Placer River Trail Bridge through image-based 3D modelling. Structure and Infrastructure Engineering, 14(1), 124-136.
50. Kim, H., Lee, J., Ahn, E., Cho, S., Shin, M., & Sim, S. H. (2017). Concrete crack identification using a UAV incorporating hybrid image processing. Sensors, 17(9), 2052.
51. Pepi, C., Gioffrè, M., Comanducci, G., Cavalagli, N., Bonaca, A., & Ubertini, F. (2017). Dynamic characterization of a severely damaged historic masonry bridge. Procedia engineering, 199, 3398-3403.
52. Duque, L., Seo, J., & Wacker, J. (2018). Bridge deterioration quantification protocol using UAV. Journal of Bridge Engineering, 23(10), 04018080.
53. Harrington, J. (2019). In Hurricane Barry's wake, here are the worst floods in American history. https://www.usatoday.com/story/news/weather/2019/07/17/worst-floods-in-american-history/39692839/
54. Alptekin, A., & Yakar, M. (2021). İçel İli jeolojisine ve jeolojik sorunlarına genel bir bakış. İçel Dergisi, 1(1), 27-30.
55. Kanun, E., Alptekin, A., & Yakar, M. (2021). Documentation of cultural heritage by photogrammetric methods: a case study of Aba's Monumental Tomb. Intercontinental Geoinformation Days, 3, 168-171.
56. ICOMOS-ISCS (2008). International Council on Monuments and Sites—International Scientific Committee for Stone Illustrated Glossary on Stone Deterioration Patterns. 2008
57. Karataş, L. (2016). Mardin Kentsel Sit Alanındaki İbadet Yapılarında Malzeme Kullanımı ve Sorunları Üzerine Bir Araştırma (Master's Thesis, Uludağ University, Fen Bilimleri Enstitüsü, Bursa, 340p).
58. Kusak, L., Unel, F. B., Alptekin, A., Celik, M. O., & Yakar, M. (2021). Apriori association rule and K-means clustering algorithms for interpretation of pre-event landslide areas and landslide inventory mapping. Open Geosciences, 13(1), 1226-1244.
59. Ünel, F. B., Kuşak, L., Çelik, M., Alptekin, A., & Yakar, M. (2020). Kıyı çizgisinin belirlenerek mülkiyet durumunun incelenmesi. Türkiye Arazi Yönetimi Dergisi, 2(1), 33-40.
60. Alptekin, A., & Yakar, M. (2020). Determination of pond volume with using an unmanned aerial vehicle. Mersin Photogrammetry Journal, 2(2), 59-63.
61. Şasi, A., & Yakar, M. (2017). Photogrammetric modelling of sakahane masjid using an unmanned aerial vehicle. Turkish Journal of Engineering, 1(2), 82-87.
62. Kanun, E., Alptekin, A., Karataş, L., & Yakar, M. (2022). The use of UAV photogrammetry in modeling ancient structures: A case study of "Kanytellis". Advanced UAV, 2(2), 41-50.
63. Yakar, M., Ulvi, A., Yiğit, A. Y., & Alptekin, A. (2022). Discontinuity set extraction from 3D point clouds obtained by UAV Photogrammetry in a rockfall site. Survey Review, 1-13.
64. Karataş, L., Alptekin, A., Karabacak, A., & Yakar, M. (2022). Detection and documentation of stone material deterioration in historical masonry buildings using UAV photogrammetry: A case study of

Mersin Sarisih Inn. Mersin Photogrammetry Journal, 4(2), 53-61.
65. Yakar, M., Yılmaz, H. M., & Mutluoğlu, Ö. (2009). Hacim Hesaplamalarında Lazer Tarama ve Yersel Fotogrametrinin Kullanılması. TMMOB Harita ve Kadastro Mühendisleri Odası 12. Türkiye Harita Bilimsel ve Teknik Kurultayı.
66. Yakar, M., Yilmaz, H. M., & Mutluoglu, O. (2014). Performance of Photogrammetric and Terrestrial Laser Scanning Methods in Volume Computing of Excavtion and Filling Areas. Arabian Journal for Science and Engineering, 39(1), 387-394.
67. Doğan, Y., & Yakar, M. (2018). GIS and three-dimensional modeling for cultural heritages. International Journal of Engineering and Geosciences, 3(2), 50-55.
68. Çelik, M. Ö., Alptekin, A., Ünel, F. B., Kuşak, L., & Kanun, E. (2020). The effect of different flight heights on generated digital products: DSM and Orthophoto. Mersin Photogrammetry Journal, 2(1), 1-9.
69. Cárdenes, V., Cnudde, J. P., Wichert, J., Large, D., López-Mungira, A., & Cnudde, V. (2016). Roofing slate standards: A critical review. Construction and Building Materials, 115, 93-104.
70. Waragai, T., & Hiki, Y. (2019). Influence of microclimate on the directional dependence of sandstone pillar weathering in Angkor Wat temple, Cambodia. Progress in Earth and Planetary Science, 6(1), 1-14.
71. Lubelli, B., & Nijland, T. G. (2014). Damage mechanism in Tournai limestone–the case of the tomb of admiral tromp in the old Church of Delft (the Netherlands). Journal of cultural heritage, 15(3), 313-317.